

Addressing leakage and mode suppression in angular power spectrum estimation for gravitational-wave backgrounds using pulsar timing arrays

Deepali Agarwal* and Joseph D. Romano†

*Department of Physics and Astronomy, University of Texas Rio Grande Valley,
One West University Boulevard, Brownsville, TX 78520, USA*

Yacine Ali-Haïmoud‡

*Center for Cosmology and Particle Physics, Department of Physics,
New York University, New York, New York 10003, USA*

Tristan L. Smith§

Department of Physics and Astronomy, Swarthmore College, 500 College Ave., Swarthmore, PA 19081, USA

Mapping gravitational-wave background (GWB) anisotropy with pulsar timing arrays (PTAs) is affected by (harmonic space) mode suppression and mode coupling arising from an array’s nonuniform sky response. Due to computational limitations, one must truncate spherical harmonic expansions at a finite multipole for recovery, ℓ_{\max}^{rec} , often chosen to equal $\ell_{\max}^{N_{\text{pair}}} \equiv \text{int}[\sqrt{N_{\text{pair}}} - 1]$, where $N_{\text{pair}} \equiv N_{\text{psr}}(N_{\text{psr}} - 1)/2$ is the number of distinct pulsar pairs in an array comprised of N_{psr} pulsars. This choice is motivated by the counting argument that cross-correlations provide at most N_{pair} independent pieces of information. Here, we explicitly obtain the multipole value (denoted ℓ_{\max}^{res}) that corresponds (approximately) to the maximum informative angular scale of an array of pulsars. This value is defined by the requirement that spherical harmonic expansions out to ℓ_{\max}^{res} approximately span the space of “observable skies” extracted by the array, which is encoded in the N_{pair} eigenmaps of the Fisher information matrix. The value of ℓ_{\max}^{res} depends on specifics of the PTA configuration. We also explicitly show that GWB power contained in multipoles $\ell \gtrsim \ell_{\max}^{\text{res}}$ do not significantly affect analyses that use expansions out to ℓ_{\max}^{res} , due to the mode suppression (i.e., low-pass filtering) induced by the PTA response to the GWB. However, truncating spherical harmonic expansions at $\ell_{\max}^{\text{rec}} < \ell_{\max}^{\text{res}}$ leads to leakage of small-scale angular power from multipoles $\ell_{\max}^{\text{rec}} < \ell \leq \ell_{\max}^{\text{res}}$. Nonetheless, even if we use ℓ_{\max}^{res} for recovery, the standard frequentist estimator of the angular power spectrum components C_ℓ is still biased due to modes that are not observable by the array. Although we can (partially) debias the standard estimator—improving its agreement with an injected angular power spectrum—this reduction in bias comes at the expense of an increase in variance, with especially large variances arising for poorly constrained modes, $\ell \gg \ell_{\text{eff}}$. The results of our analyses strongly advocate for: (i) using ℓ_{\max}^{res} for PTA analyses involving spherical harmonic expansions, and (ii) using the debiased standard estimator for C_ℓ recovery, but only out to multipoles $\ell < \ell_{\text{eff}} (\ll \ell_{\max}^{\text{res}})$ corresponding to sufficiently constrained modes.

I. INTRODUCTION

Any attempt to infer the angular power spectrum of a stochastic gravitational-wave background (GWB) using pulsar timing array (PTA) data must contend with the fact that the response of the array of pulsars to the background provides only partial information of the distribution of GW power on the sky. More specifically, for a PTA comprised of N_{psr} pulsars, at most $N_{\text{pair}} \equiv N_{\text{psr}}(N_{\text{psr}} - 1)/2$ pieces of information are extractable from the N_{pair} distinct cross-correlation measurements of the timing residuals from pairs of pulsars. This information is encoded most directly in the N_{pair} eigenmaps of the Fisher information matrix, which span the space of “observable skies”, as described in detail in Ali-Haïmoud et al. [1, 2].

When modeling an anisotropic GWB, it is often convenient to expand the GW power on the sky $P(\hat{\Omega})$ in terms of spherical harmonics $Y_{\ell m}(\hat{\Omega})$. As we will show in Sec. III, if we choose our ℓ_{\max} for recovery (denoted ℓ_{\max}^{rec}) to be sufficiently large, then the set of spherical harmonics out to ℓ_{\max}^{rec} can also be used to *approximately* span the space of observable skies for our particular PTA. The threshold value that ℓ_{\max}^{rec} needs to exceed (denoted ℓ_{\max}^{res}) depends on specifics of the PTA configuration. It can be determined by the requirement that we are able to reconstruct a sufficient number (e.g., 90%) of the N_{pair} eigenvectors of the Fisher information matrix to a sufficient accuracy (e.g.,

* deepali.agarwal@utrgv.edu

† joseph.romano@utrgv.edu

‡ yah2@nyu.edu

§ tsmith2@swarthmore.edu

Notation	Definition
ℓ_{\max}^{gwb}	maximum ℓ -value for the true distribution of GW power on the sky (unknown)
ℓ_{\max}^{rec}	maximum ℓ -value used for the recovered distribution of GW power (our signal model)
ℓ_{\max}^{res}	ℓ -value corresponding to the max angular resolution of a PTA (configuration and accuracy dependent)
ℓ_{eff}	ℓ -value corresponding to the effective angular resolution of a PTA (configuration and accuracy dependent)
$\ell_{\max}^{N_{\text{pair}}}$	max ℓ -value for which the total number of SpH modes $\{\ell, m\}$ is $\leq N_{\text{pair}}$, i.e., $\ell_{\max}^{N_{\text{pair}}} = \text{int}[\sqrt{N_{\text{pair}} - 1}]$
ℓ_{\max}^{nn}	max ℓ -value defined by angular separation δ_{nn} (in deg) of nearest-neighbor pulsar pair, i.e., $\ell_{\max}^{\text{nn}} = 180^\circ/\delta_{\text{nn}}$

TABLE I. Multipoles corresponding to different angular scales discussed in this paper.

95% match) using spherical harmonics out to ℓ_{\max}^{res} . This value of ℓ_{\max} allows us to approximately capture the smallest angular scales accessible to the array. A similar idea has been recently proposed by Grunthal et al. [3] in the context of point-source reconstruction using the spherical harmonic expansions. (See Table I for definitions of spherical harmonic multipoles corresponding to different angular scales.)

Note, however, that if we simply set ℓ_{\max}^{rec} equal to that value of ℓ_{\max} for which the total number of spherical harmonic modes $\{\ell, m\}$ out to ℓ_{\max} is $\leq N_{\text{pair}}$ (denoted $\ell_{\max}^{N_{\text{pair}}}$), then we will typically not be able to reconstruct with sufficient accuracy a sufficient number of the eigenvectors of the Fisher information matrix. Using too small a value for ℓ_{\max}^{rec} leads to excessive leakage of small-scale angular power, as shown recently in Ref. [4]. But as hinted at in [4], this excess leakage of power is simply an artifact of the choice of $\ell_{\max}^{N_{\text{pair}}}$ for recovery. The excess leakage can be removed by using $\ell_{\max}^{\text{rec}} \geq \ell_{\max}^{\text{res}}$ as stated above. These claims are verified using numerical simulations and analytical calculations detailed in Secs. IV and V.

In Secs. III and IV, we also explain how leakage is due to mode coupling, which manifests itself as a non-spherically-symmetric Fisher matrix in the pixel basis. In addition, we point out how mode suppression limits the leakage of small-scale angular power from the true GWB power distribution. This means that even if the GWB has power out to ℓ_{\max}^{gwb} of order several hundred or more (assuming a constant angular power spectrum), the response of a PTA acts much like a low-pass filter of the GWB power, effectively restricting the observable multipoles to $\ell \leq \ell_{\max}^{\text{res}}$. Finally, we show that even if we use a sufficiently large ℓ_{\max}^{rec} , the standard frequentist estimator of the angular power spectrum C_ℓ is still biased due to modes that are not observable by the array. It turns out that we can debias the standard estimator, reducing its bias at the expense of an increase in variance. But the increase in variance becomes especially large for the most poorly constrained modes.

The rest of the paper is organized as follows: In Sec. II, we introduce the mathematical formalism needed to discuss the frequentist cross-correlation estimators of the angular power spectrum C_ℓ used for our analyses. Sections III and IV presents the main results, which we have already highlighted above. In Sec. V, we show how these results depend on specifics of the PTA configuration. Finally in Sec. VI, we conclude with a brief summary and discussion of possible extensions of this work. Appendix A contains some mathematical details regarding the statistical properties of the various estimators used in this paper. Appendix B demonstrates that, in the absence of mode coupling, unmodeled GWB angular scales do not bias the angular power spectrum estimator. And App. C discusses the impact of the choice of the condition number for regularizing matrix inversion on C_ℓ recovery.

II. MATHEMATICAL PRELIMINARIES

A. Map-making using PTA data

As mentioned in the introduction, we are interested in searching for an anisotropic GWB. Assuming that an unpolarized GWB signal can be characterized as a stationary Gaussian process, the Fourier coefficients of the GW strain satisfy:

$$\langle \tilde{h}_A(f, \hat{\Omega}) \tilde{h}_{A'}^*(f', \hat{\Omega}') \rangle = \delta_{AA'} \delta^2(\hat{\Omega}, \hat{\Omega}') \delta(f - f') P(f, \hat{\Omega}), \quad (2.1)$$

where $P(f, \hat{\Omega})$ is the one-sided power spectral density (PSD), which is the primary quantity probed by GW experiments. For a broadband source, the frequency and direction dependence of the PSD is often factorized as

$$P(f, \hat{\Omega}) = H(f) P(\hat{\Omega}). \quad (2.2)$$

Since our focus is exclusively on anisotropy, we set $H(f) = 1$ in the following discussion, which is equivalent to estimating only $P(\hat{\Omega})$.

For an extended distribution of GWB power on the sky, it is convenient to decompose the angular dependence of $P(\hat{\Omega})$ in a spherical harmonic (SpH) basis as

$$P(\hat{\Omega}) = \sum_{\ell=0}^{\ell_{\max}^{\text{gwb}}} \sum_{m=-\ell}^{\ell} P_{\ell m} Y_{\ell m}(\hat{\Omega}), \quad (2.3)$$

where $P_{\ell m}$ are the spherical harmonic coefficients of $P(\hat{\Omega})$ and $Y_{\ell m}(\hat{\Omega})$ are the corresponding basis functions. We have assumed that the GW power has support on angular scales $0 \leq \ell \leq \ell_{\max}^{\text{gwb}}$ (in principle, ℓ_{\max}^{gwb} can be arbitrarily large). For a statistically-isotropic GWB (which has no preferred direction), and assuming that the monopole has been perfectly subtracted, the spherical harmonic coefficients are fully characterized by the angular power spectrum components C_ℓ defined via

$$\langle P_{\ell m} \rangle_P = 0, \quad \langle P_{\ell m} P_{\ell' m'}^* \rangle_P = C_\ell \delta_{\ell\ell'} \delta_{mm'}, \quad (2.4)$$

where $\langle \rangle_P$ denotes ensemble average over different $P_{\ell m}$ realizations corresponding to a fixed set of C_ℓ .

In PTA experiments, the spherical harmonic components and angular power spectrum of an anisotropic GWB are estimated from cross-correlations ρ_{ab} of timing residuals between distinct pulsar pairs, labeled by $a < b$. The expectation value of the measured cross-correlation ρ_{ab} is related to $P(\hat{\Omega})$ via [5, 6]:

$$\langle \rho_{ab} \rangle = \int d^2\hat{\Omega} \gamma_{ab}(\hat{\Omega}) P(\hat{\Omega}) = \sum_{\ell=0}^{\ell_{\max}^{\text{gwb}}} \sum_{m=-\ell}^{\ell} \gamma_{ab,\ell m} P_{\ell m}, \quad (2.5)$$

where

$$\gamma_{ab}(\hat{\Omega}) \equiv \sum_{A=+,\times} F^A(\hat{p}_a, \hat{\Omega}) F^A(\hat{p}_b, \hat{\Omega}), \quad \gamma_{ab,\ell m} \equiv \int d^2\hat{\Omega} \gamma_{ab}(\hat{\Omega}) Y_{\ell m}(\hat{\Omega}). \quad (2.6)$$

Here $F^A(\hat{p}_a, \hat{\Omega})$ denotes the response of pulsar a to a GW with polarization A propagating in direction $\hat{\Omega}$. The functions $\gamma_{ab}(\hat{\Omega})$ can be written explicitly as simple functions of the dot products between \hat{p}_a , \hat{p}_b , and $\hat{\Omega}$, as shown in [1]. The quantity $\gamma_{ab,00}$ corresponds to the Hellings-Downs correlation [7], which depends only on the separation angle between \hat{p}_a and \hat{p}_b . (Here, \hat{p}_a denotes the unit vector pointing from Earth to pulsar a .)

It what follows, we will use the nomenclature of [1, 2] and refer to the $\gamma_{ab}(\hat{\Omega})$ as *pairwise timing response* (PTR) maps. We note that the PTRs are closely related to—but different from—the so-called *overlap reduction functions* (ORFs) [8–10], which are the angular integrals of the PTRs multiplied by the GWB power [11], and thus measure the “overlap” of the instrumental response with the GWB sky.

To reconstruct the spherical harmonic coefficients $P_{\ell m}$ from the data, we assume that the signal has support for multipoles $0 \leq \bar{\ell} \leq \bar{\ell}_{\max}^{\text{rec}}$. (Note that we are using barred indices $(\bar{\ell}, \bar{m})$ to denote spherical harmonic coefficients for the recovered signal as opposed to unbarred indices (ℓ, m) for the true GWB.) Assuming that the cross-correlations are described by a Gaussian distribution, the likelihood function is maximized with respect to $P_{\bar{\ell}\bar{m}}$ when [3, 5, 6, 12–14]:

$$\hat{P}_{\bar{\ell}\bar{m}} = \sum_{\bar{\ell}'\bar{m}'} (\mathcal{F}^{-1})_{\bar{\ell}\bar{m},\bar{\ell}'\bar{m}'} X_{\bar{\ell}'\bar{m}'}, \quad (2.7)$$

where the “dirty map” $X_{\bar{\ell}'\bar{m}'}$ and spherical harmonic coefficients $\mathcal{F}_{\bar{\ell}\bar{m},\bar{\ell}'\bar{m}'}$ of the Fisher information matrix \mathcal{F} are defined via

$$X_{\bar{\ell}\bar{m}} \equiv \sum_{a<b} \frac{\gamma_{ab,\bar{\ell}\bar{m}}^* \rho_{ab}}{\sigma_{ab}^2}, \quad \mathcal{F}_{\bar{\ell}\bar{m},\bar{\ell}'\bar{m}'} \equiv \sum_{a<b} \frac{\gamma_{ab,\bar{\ell}\bar{m}}^* \gamma_{ab,\bar{\ell}'\bar{m}'}}{\sigma_{ab}^2}. \quad (2.8)$$

Here, σ_{ab}^2 denotes the variance of cross-correlations ρ_{ab} . The noise covariance of the “clean map” estimator $\hat{P}_{\bar{\ell}\bar{m}}$ is given by $\mathcal{F}_{\bar{\ell}\bar{m},\bar{\ell}'\bar{m}'}^{-1}$.

We note that (2.8) implicitly assumes the *weak-signal limit*, for which the timing noise is dominated by intrinsic pulsar noise. This implies, in particular, that the covariance matrix of the cross-correlations ρ_{ab} is diagonal. In general, a non-negligible GWB (in particular its monopole, which should dominate over anisotropies) would imply non-zero off-diagonal correlations between different pulsar pairs, involving the Hellings-and-Downs function, see e.g. [1]. If we are able to measure the monopole sufficiently accurately, then this monopole-dependent, non-diagonal covariance

matrix would replace σ_{ab}^2 in the definition (2.8) of the “dirty map” and Fisher matrix, see e.g., [4, 14]. We will not consider this particular modification of (2.8) for our analyses.

Finally, we note that, in practice, the Fisher matrix \mathcal{F} is ill-conditioned whenever the number of modes we are trying to recover is greater than the N_{pair} cross-correlation measurements that we have to work with. For this case, \mathcal{F} must be regularized to obtain a pseudo-inverse \mathcal{F}^+ . The clean map estimator (2.7) then becomes [3, 4, 13, 14]

$$\hat{P}_{\bar{\ell}\bar{m}} = \sum_{\bar{\ell}'\bar{m}'} \mathcal{F}_{\bar{\ell}\bar{m},\bar{\ell}'\bar{m}'}^+ X_{\bar{\ell}'\bar{m}'} . \quad (2.9)$$

In this article, we employ a singular-value-decomposition (SVD)-based regularization scheme. The Fisher matrix is decomposed as

$$\mathcal{F} = \mathbf{U} \cdot \mathbf{\Sigma} \cdot \mathbf{V}^\dagger , \quad (2.10)$$

where \mathbf{U} and \mathbf{V} are unitary matrices, and $\mathbf{\Sigma}$ is a diagonal matrix with elements $\Sigma_{ij} = s_i \delta_{ij}$, with s_i denoting the singular values. We note that for a square Hermitian matrix (as is the case for the Fisher matrix), the \mathbf{U} and \mathbf{V} matrices coincide and the SVD decomposition reduces to an eigenvalue-eigenvector decomposition. To construct the pseudo-inverse, we introduce a condition number threshold κ . The pseudo-inverse is defined as

$$\mathcal{F}^+ = \mathbf{V} \cdot \mathbf{\Sigma}^+ \cdot \mathbf{U}^\dagger , \quad (2.11)$$

where

$$(\mathbf{\Sigma}^+)_{ij} = \delta_{ij} \begin{cases} 1/s_i & \text{for } s_i > \max[s_i]/\kappa \\ 0 & \text{for } s_i \leq \max[s_i]/\kappa \end{cases} . \quad (2.12)$$

In other words, $\mathbf{\Sigma}^+$ contains the inverse of the singular values for the retained modes, while modes with smaller singular values are set to zero for $\mathbf{\Sigma}^+$.

The necessity of using the pseudo-inverse \mathcal{F}^+ instead of true inverse \mathcal{F}^{-1} of the Fisher matrix implies that the $\hat{P}_{\bar{\ell}\bar{m}}$ estimators are biased [4, 13, 14], as shown explicitly in App. A, see (A3) and (A4). This bias propagates to the standard frequentist estimator $\hat{C}_{\bar{\ell}}$ of the angular power spectrum $C_{\bar{\ell}}$, as we will show in the following subsection. The bias and variance of these estimators depend on the condition number threshold: higher thresholds reduce the bias but increase the variance, as we discuss in App. C.

B. Standard estimator for the angular power spectrum

Given the clean map estimators $\hat{P}_{\bar{\ell}\bar{m}}$ defined in (2.9), we can then define an estimator of the angular power spectrum [4–6, 13]

$$\hat{C}_{\bar{\ell}} \equiv \frac{1}{2\bar{\ell} + 1} \sum_{\bar{m}} |\hat{P}_{\bar{\ell}\bar{m}}|^2 - N_{\bar{\ell}} . \quad (2.13)$$

Note that we need to subtract a noise bias term [13]

$$N_{\bar{\ell}} \equiv \frac{1}{2\bar{\ell} + 1} \sum_{\bar{m}} \mathcal{N}_{\bar{\ell}\bar{m},\bar{\ell}\bar{m}} , \quad \mathcal{N}_{\bar{\ell}\bar{m},\bar{\ell}'\bar{m}'} \equiv (\mathcal{F}^+ \cdot \mathcal{F} \cdot \mathcal{F}^{+\dagger})_{\bar{\ell}\bar{m},\bar{\ell}'\bar{m}'} , \quad (2.14)$$

which is derived in App. A. In an ideal experiment, one would like to reconstruct as many modes as possible. However, $\ell_{\text{max}}^{\text{rec}}$ is limited by computational constraints or by the intrinsic information content of the data: finite-width point spread functions and increasing noise at smaller angular scales limit the number of recoverable modes. These cases will be discussed in the next section.

If \mathcal{F} is ill-conditioned and $\ell_{\text{max}}^{\text{rec}} < \ell_{\text{max}}^{\text{gwb}}$, then $\hat{C}_{\bar{\ell}}$ will be biased away from its true value, even after subtracting away $N_{\bar{\ell}}$ as in (2.13) [4, 13]. As shown in (A6)

$$\langle\langle \hat{C}_{\bar{\ell}} \rangle\rangle_P = \sum_{\ell'} M_{\bar{\ell}\ell'} C_{\ell'} , \quad (2.15)$$

where [4, 15]

$$M_{\bar{\ell}\ell'} \equiv \frac{1}{2\bar{\ell} + 1} \sum_{\bar{m}\bar{m}'} |K_{\bar{\ell}\bar{m},\ell'm'}|^2 , \quad K_{\bar{\ell}\bar{m},\ell'm'} \equiv \sum_{\bar{\ell}'\bar{m}'} \mathcal{F}_{\bar{\ell}\bar{m},\bar{\ell}'\bar{m}'}^+ \mathcal{F}_{\bar{\ell}'\bar{m}',\ell'm'} . \quad (2.16)$$

This implies that the fractional bias in the reconstructed angular power spectrum is

$$b_{\bar{\ell}} \equiv \frac{\langle\langle \hat{C}_{\bar{\ell}} \rangle\rangle_P - C_{\bar{\ell}}}{C_{\bar{\ell}}} = \sum_{\ell'} \frac{M_{\bar{\ell}\ell'} C_{\ell'}}{C_{\bar{\ell}}} - 1. \quad (2.17)$$

Note that \mathbf{M} and \mathbf{K} are rectangular matrices if $\ell_{\max}^{\text{rec}} \neq \ell_{\max}^{\text{gwb}}$. The behavior of the bias matrix \mathbf{M} for a given pulsar configuration is discussed at the end of Sec. IV A, where we consider *debiasing* the standard estimator (2.13) of the angular power spectrum.

Finally, using Isserlis's theorem and the statistical properties of the estimators given in App. A, we can also derive the covariance matrix of the $\hat{C}_{\bar{\ell}}$ estimators [15]. As shown in more detail in App. A, we find

$$\text{Cov}(\hat{C}_{\bar{\ell}}, \hat{C}_{\bar{\ell}'}) = \frac{2}{(2\bar{\ell} + 1)(2\bar{\ell}' + 1)} \sum_{\bar{m}\bar{m}'} |C_{\bar{\ell}\bar{m},\bar{\ell}'\bar{m}'} + \mathcal{N}_{\bar{\ell}\bar{m},\bar{\ell}'\bar{m}'}|^2, \quad (2.18)$$

where

$$C_{\bar{\ell}\bar{m},\bar{\ell}'\bar{m}'} \equiv \sum_{\ell m} K_{\bar{\ell}\bar{m},\ell m} K_{\bar{\ell}'\bar{m}',\ell m}^* C_{\ell}, \quad (2.19)$$

and $\mathcal{N}_{\bar{\ell}\bar{m},\bar{\ell}'\bar{m}'}$ is given by (2.14). We note that $C_{\bar{\ell}\bar{m},\bar{\ell}'\bar{m}'}$ involves a sum over C_{ℓ} and gives rise to *cosmic variance*. In the weak-signal limit, the covariance in (2.18) is dominated by the noise contribution $\mathcal{N}_{\bar{\ell}\bar{m},\bar{\ell}'\bar{m}'}$.

Although we have assumed the weak-signal limit to derive these expressions, the analyses presented in Sec. IV will, for the sake of simplicity, keep only the cosmic variance part of the covariance matrix (the noiseless case). While this is not self-consistent, it is similar to the noiseless case of [4] against which we wish to compare our results. (Reference [4] also considers the effect of pulsar noise and contributions to the variance induced by the GWB itself, which we do not.) A more realistic treatment, including the contribution of pulsar noise, will be pursued in future work.

III. INFORMATIVE ANGULAR MODES IN PULSAR TIMING ARRAY DATA

The ability of a pulsar timing array to resolve angular structure in the GWB is fundamentally limited by its Fisher information. In this section, we characterize this limitation by studying properties of the Fisher information matrix, identifying an effective maximum informative multipole ℓ_{\max}^{res} . We demonstrate its impact on angular power spectrum recovery in Sec. IV.

For these analytical calculations with the Fisher matrix, we will assume that $\sigma_{ab}^2 \equiv \sigma^2 \equiv 1$, corresponding to the case where the pulsar noise is the same for all pulsars. This implies that the correlated response of the PTA to the GWB depends only the geometrical configuration of the pulsar sky locations; it is not weighted differently according to the individual pulsar noise.

A. Harmonic-space structure of the PTA Fisher matrix

In the idealized limit of infinite angular resolution, the Fisher kernel would take the form

$$\mathcal{F}(\hat{\Omega}, \hat{\Omega}') = \delta^2(\hat{\Omega}, \hat{\Omega}'). \quad (3.1)$$

(Here, we are using the word “kernel” when we think of $\mathcal{F}(\hat{\Omega}, \hat{\Omega}')$ as a function of two *continuous* directions on the sky $\hat{\Omega}$ and $\hat{\Omega}'$.) In this limit (3.1), the harmonic space representation of the Fisher kernel, defined as

$$\mathcal{F}_{\ell m, \ell' m'} \equiv \int d^2\hat{\Omega} d^2\hat{\Omega}' Y_{\ell m}(\hat{\Omega}) Y_{\ell' m'}^*(\hat{\Omega}') \mathcal{F}(\hat{\Omega}, \hat{\Omega}'), \quad (3.2)$$

satisfies

$$\mathcal{F}_{\ell m, \ell' m'} = \delta_{\ell\ell'} \delta_{mm'}. \quad (3.3)$$

So, all the multipoles up to $\ell_{\max} = \infty$ are accessible.

However, realistic experiments are limited by the finite width of the position-space Fisher kernel, which restricts sensitivity to small-scale angular features. Finite angular resolution blurs structures beyond a certain angular scale, acting as a low-pass filter.

For example, consider a spherically symmetric Fisher kernel derived for an infinite number of isotropically-distributed identical pulsars (a so-called “dense-PTA”, see Eq. (71) in Ref. [1]). By spherical symmetry, the kernel depends upon only on $\hat{\Omega} \cdot \hat{\Omega}'$, and its harmonic space representation is diagonal:

$$\mathcal{F}_{\ell m, \ell' m'} = \mathcal{F}_\ell \delta_{\ell \ell'} \delta_{m m'}, \quad (3.4)$$

where \mathcal{F}_ℓ is a monotonically decreasing function of ℓ (see Fig. 3 in Ref. [1]). We note that: (i) because $\mathcal{F}_{\ell m, \ell' m'}$ is diagonal, there is no coupling between different multipoles, and (ii) the variance of the clean map estimator scales as \mathcal{F}_ℓ^{-1} .

If we further assume statistical isotropy of the background, then there is an additional constraint: each ℓ -mode has $2\ell + 1$ independent m -modes that can be averaged together, thus reducing the growth in the variance for large ℓ values (corresponding to small angular scales). Consequently, the noise uncertainty of the angular power spectrum estimator then scales as $(2\ell + 1)^{-1/2} \mathcal{F}_\ell^{-1}$, as one can see from (A8).

In addition, realistic PTAs have responses to the GWB that are not spherically symmetric. As a result, the Fisher information matrix in both position and harmonic space has non-zero off-diagonal terms, corresponding to mode coupling between different multipoles.

To illustrate these concepts more concretely, we consider a PTA configuration consisting of 34 pulsars drawn from a statistically-uniform distribution on the sky, as shown in Fig. 1. For this configuration, the diagonal elements of the Fisher information matrix decay rapidly with increasing ℓ (see left panel of Fig. 2), indicating strong mode suppression at small angular scales. The off-diagonal elements reveal non-negligible multipole coupling, as shown in the right panel of the same figure. Both the degree of mode suppression and the strength of multipole coupling depend on specifics of the PTA configuration, as is discussed in more detail in Sec. V.

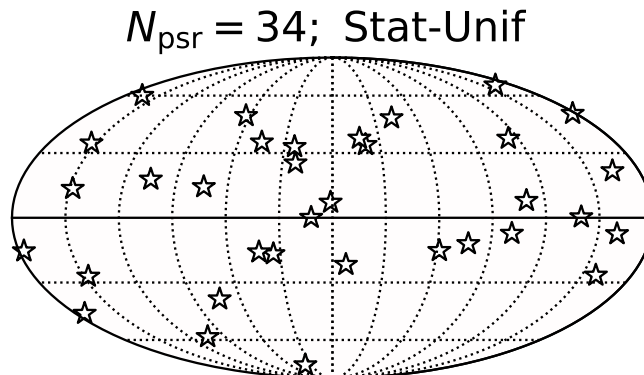


FIG. 1. Sky location of 34 pulsars drawn from a statistically-uniform distribution, used for the main analyses in Sec. IV.

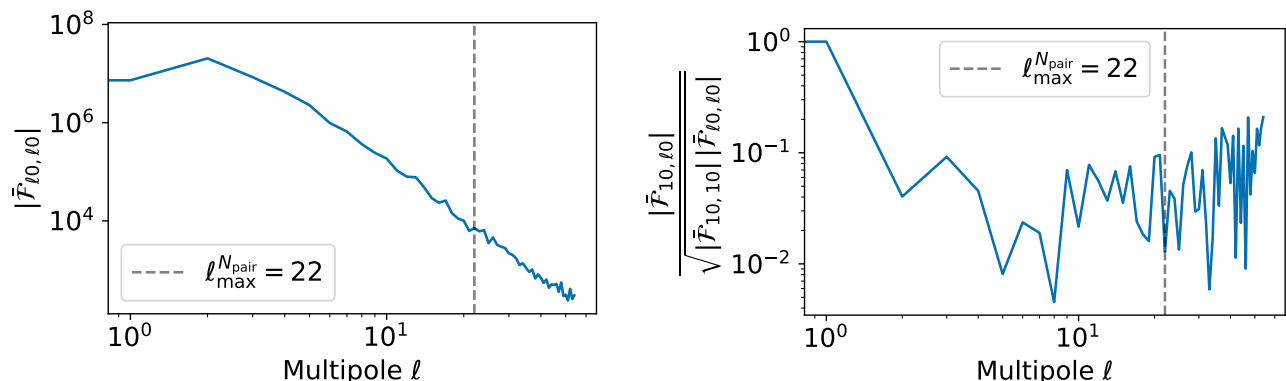


FIG. 2. Plots showing mode suppression (left panel) and mode coupling (right panel) calculated using the Fisher matrix for the $N_{\text{psr}} = 34$, Stat-Unif configuration shown in Fig. 1.

Mode suppression and coupling together limit the range of angular modes that carry significant information about the distribution of GW power. This *finite* scale, determined in the next section, naturally provides a truncation point

for harmonic space analyses and determines the bias and leakage induced from mode coupling, as discussed in the following sections.

B. Observable skies and the maximum-informative multipole ℓ_{\max}^{res}

As mentioned in Sec. I, N_{pair} cross-correlation measurements from an array of N_{psr} pulsars provide at most N_{pair} independent pieces of information about the anisotropy of the GWB (see (2.5)). This has been discussed in detail by Ali-Haïmoud et al. [1, 2]. Previous studies of anisotropy often imposed a hard cutoff on reconstructible angular scales based on counting arguments [6, 16, 17], leading to the conventional limit

$$\ell_{\max}^{N_{\text{pair}}} \equiv \text{int}[\sqrt{N_{\text{pair}}} - 1]. \quad (3.5)$$

In particular, Semenzato et al. [4] highlighted the potential of excess leakage of small-scale angular power when reconstructing the angular power spectrum of the background, truncating their spherical harmonic analysis at $\ell_{\max}^{\text{rec}} = \ell_{\max}^{N_{\text{pair}}}$. As noted by Grunthal et al. [3] in the context of point source reconstruction, this limit does not fully reflect the true angular resolution of a PTA. So, here, we ask: how large must ℓ_{\max}^{rec} be to capture nearly all of the significant information encoded in a PTA, while allowing for a regularization scheme to naturally suppress numerically unstable modes. (NOTE: In what follows, we will answer this question by doing the calculation using the Fisher information matrix in the PTR basis, since it captures most directly the N_{pair} pieces of information extracted by the pulsar pair cross-correlation measurements. But the calculation could also be done by expressing the Fisher matrix in either the pixel or SpH bases, although for those cases, one would need to use singular-value decomposition to obtain the N_{pair} eigenvectors and eigenvalues. Provided that all N_{pair} eigenmodes are fully retained, the Fisher matrix in any of these bases, in principle, contain the same information.)

To answer this question about ℓ_{\max}^{res} , we start by expressing the Fisher information matrix \mathcal{F} in the PTR basis [1, 2]:

$$\mathcal{F}_{ab,cd} \equiv \int d\hat{\Omega} \gamma_{ab}(\hat{\Omega}) \gamma_{cd}(\hat{\Omega}) \simeq \frac{4\pi}{N_{\text{pix}}} \sum_{i=1}^{N_{\text{pix}}} \gamma_{ab}(\hat{\Omega}_i) \gamma_{cd}(\hat{\Omega}_i), \quad (3.6)$$

where the PTR maps $\gamma_{ab}(\hat{\Omega})$ are defined in (2.6). (As mentioned above, we are assuming that all pulsars have the same noise, $\sigma_{ab}^2 \equiv \sigma^2 \equiv 1$.) The matrix component indices ab and cd satisfy $a < b$ and $c < d$, labeling distinct pulsar pairs. This implies that in the PTR basis $\mathcal{F}_{ab,cd}$ has dimension $N_{\text{pair}} \times N_{\text{pair}}$. (This matrix is denoted \mathcal{F}_{IJ} in [1, 2], with the indices $I = ab$, $J = cd$ labeling the distinct pulsar pairs.)

To evaluate the integral in (3.6), we need to pixelize the sky. We choose N_{pix} to be sufficiently large so that the sky integral can be well-approximated by a discrete sum, with results that converge as the number of pixels increase. For all the analyses that we will describe in this paper, this requirement is satisfied if $N_{\text{pix}} = 12\,288$, corresponding to $N_{\text{side}} = 32$ in HEALPix[18], [19, 20]. This is shown in the left panel of Fig. 3, where we compare the N_{pair} eigenvalues for the Fisher matrix $\mathcal{F}_{ab,cd}$ expanded in terms of pixels for different choices for N_{side} . This is for the PTA configuration shown in Fig. 1, which has $N_{\text{psr}} = 34$ pulsars and $N_{\text{pair}} = 561$ eigenvectors and eigenvalues. The spectra of eigenvalues converge to the true spectrum as we increase N_{side} from 8 to 16 to 32. So we will use $N_{\text{side}} = 32$ for all subsequent analyses in this paper, unless explicitly indicated otherwise.

We can also approximate the integral by performing a sum over the spherical harmonic components of the PTR sky maps:

$$\mathcal{F}_{ab,cd}^{\text{sph}} \equiv \sum_{\bar{\ell}=0}^{\ell_{\max}^{\text{rec}}} \sum_{\bar{m}=-\bar{\ell}}^{\bar{\ell}} \gamma_{ab,\bar{\ell}\bar{m}} \gamma_{cd,\bar{\ell}\bar{m}}^*, \quad \text{where} \quad \gamma_{ab,\bar{\ell}\bar{m}} \equiv \frac{4\pi}{N_{\text{pix}}} \sum_{i=1}^{N_{\text{pix}}} \gamma_{ab}(\hat{\Omega}_i) Y_{\bar{\ell}\bar{m}}(\hat{\Omega}_i). \quad (3.7)$$

This sum for $\mathcal{F}_{ab,cd}^{\text{sph}}$ is over $\bar{\ell}$ values out to some ℓ_{\max}^{rec} for recovery, which we recommend be $\geq \ell_{\max}^{\text{res}}$, where ℓ_{\max}^{res} captures (approximately) the maximum-informative multipole of the GWB observable by the PTA.

More precisely, we define ℓ_{\max}^{res} as the minimum value of ℓ_{\max} for which $\geq 90\%$ of the N_{pair} eigenvectors of $\mathcal{F}_{ab,cd}^{\text{sph}}$ have a match ≥ 0.95 with the corresponding N_{pair} eigenvectors of the Fisher matrix $\mathcal{F}_{ab,cd}$ (expanded in terms of pixels for $N_{\text{side}} = 32$, as discussed above). Here, the match between two vectors \mathbf{A} and \mathbf{B} is defined by

$$\text{Match}(\mathbf{A}, \mathbf{B}) \equiv \frac{|\mathbf{A} \cdot \mathbf{B}|}{\sqrt{(\mathbf{A} \cdot \mathbf{A})(\mathbf{B} \cdot \mathbf{B})}}, \quad (3.8)$$

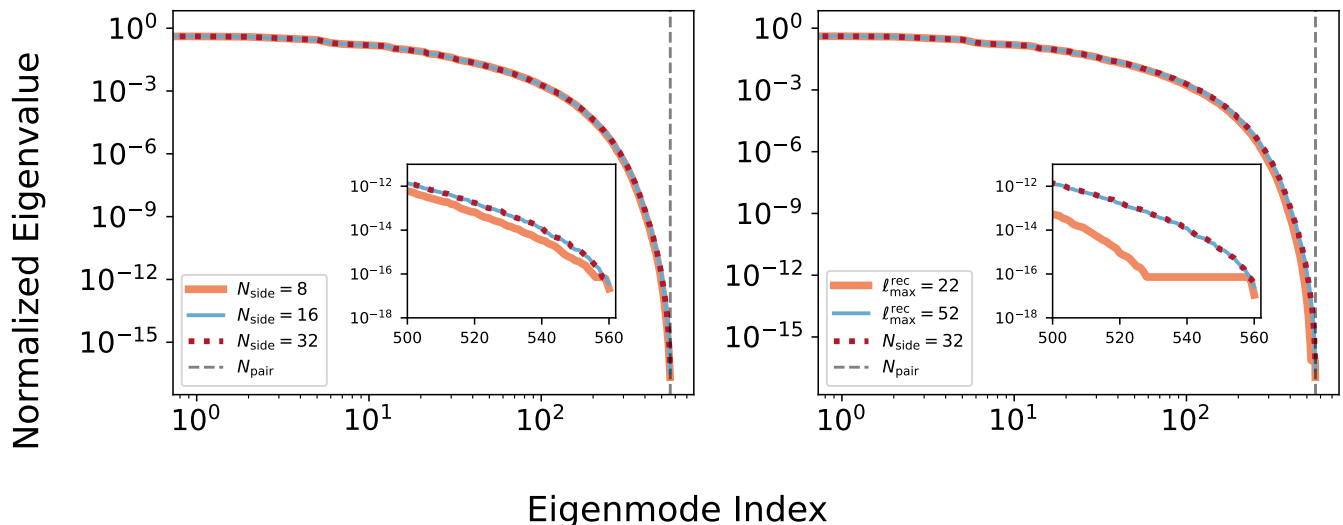


FIG. 3. Eigenvalue spectrum of the Fisher matrix $\mathcal{F}_{ab,cd}$ in the PTR basis, expanded in terms of pixels for different choices of N_{side} (left panel); and expanded in terms of spherical harmonics for different choices of $\ell_{\text{max}}^{\text{rec}}$ (right panel). These plots correspond to the PTA configuration shown in Fig. 1. Insets in both panels show zoomed-in eigenvalues for large eigenmode indices, which correspond to the smallest eigenvalues. Note that an $N_{\text{side}} = 32$ pixel expansion (left panel) and an $\ell_{\text{max}}^{\text{rec}} = 52$ SpH expansion (right panel) converges to the true eigenvalue spectrum, while an $N_{\text{side}} = 8$ pixel expansion and an $\ell_{\text{max}}^{\text{rec}} = 22$ SpH expansion have not converged to the true spectrum.

where $\mathbf{A} \cdot \mathbf{B}$ denotes the usual Euclidean inner product of two vectors as a sum of the product of their components with respect to an orthonormal basis. Note that we have included an absolute value sign in the definition of the match to allow for a possible \pm ambiguity in the definition of the eigenvectors.

The result of this match calculation leads to $\ell_{\text{max}}^{\text{res}} = 52$ for the $N_{\text{psr}} = 34$ PTA configuration shown in Fig. 1. Details of this calculation are illustrated in Fig. 4, including a comparison (in the left panel) of two different analyses: one which chooses $\ell_{\text{max}}^{\text{rec}} = \ell_{\text{max}}^{\text{res}} = 52$ (the maximum informative multipole for the array), while the other chooses $\ell_{\text{max}}^{\text{rec}} = \ell_{\text{max}}^{N_{\text{pair}}} = 22$ (the conventional limit for 34 pulsars). By choosing $\ell_{\text{max}}^{\text{rec}} = 52$ (blue circles), we obtain very good approximations of the Fisher matrix eigenvectors, thus allowing us to recover the majority of the N_{pair} informative modes. Choosing $\ell_{\text{max}}^{\text{rec}} = \ell_{\text{max}}^{N_{\text{pair}}} = 22$ (orange triangles), on the other hand, leads to poor approximations of these eigenvectors. In the right panel of Fig. 4, we plot the fraction of modes with match ≥ 0.95 as a function of $\ell_{\text{max}}^{\text{rec}}$. The curve exceeds 0.90 when $\ell_{\text{max}}^{\text{rec}} = 52$ (vertical red line), identifying $\ell_{\text{max}}^{\text{res}} = 52$ as the maximum informative angular scale for the PTA configuration in Fig. 1. In addition, as shown in the right panel of Fig. 3, $\ell_{\text{max}}^{\text{rec}} = 52$ (blue solid) consistently recovers the true eigenvalue spectrum (red dashed), whereas $\ell_{\text{max}}^{\text{rec}} = 22$ (orange solid) does not.

IV. DEMONSTRATIONS OF LEAKAGE AND MODE SUPPRESSION

In this section, we illustrate the impact of mode suppression and mode coupling, and compare the reconstruction of the angular power spectrum with a PTA when analyses are truncated at $\ell_{\text{max}}^{\text{rec}}$ equal to either $\ell_{\text{max}}^{N_{\text{pair}}}$ or $\ell_{\text{max}}^{\text{res}}$. For the following analyses we will assume that the pulsar noise is zero, i.e., $\sigma_{ab}^2 = 0$ for all pulsar pairs. As mentioned earlier this allows us to easily compare our results to [4], which also consider leakage of small-scale angular power in this context (Ref. [4] also considers noise-full analyses).

We note that setting $\sigma_{ab}^2 = 0$ is well defined and does not lead to ill-defined behavior in the equations. This is because the clean map estimator (2.7) is independent of σ^2 once the same noise-level limit is imposed. In this limit, its noise variance vanishes as the Fisher information matrix (2.8) diverges. As a result, the signal contribution to both the standard C_ℓ estimator (2.13) and its covariance (2.18) remain unchanged, while the noise contribution to the bias (equal to the clean map noise variance) and covariance are identically zero. For this reason, we refer to this noise-free case as the best-case scenario for angular power spectrum estimation. In the presence of (unknown) noise, obtaining an unbiased estimator becomes more challenging—particularly due to limitations on the reconstructible modes—but this regime is beyond the scope of the present work.

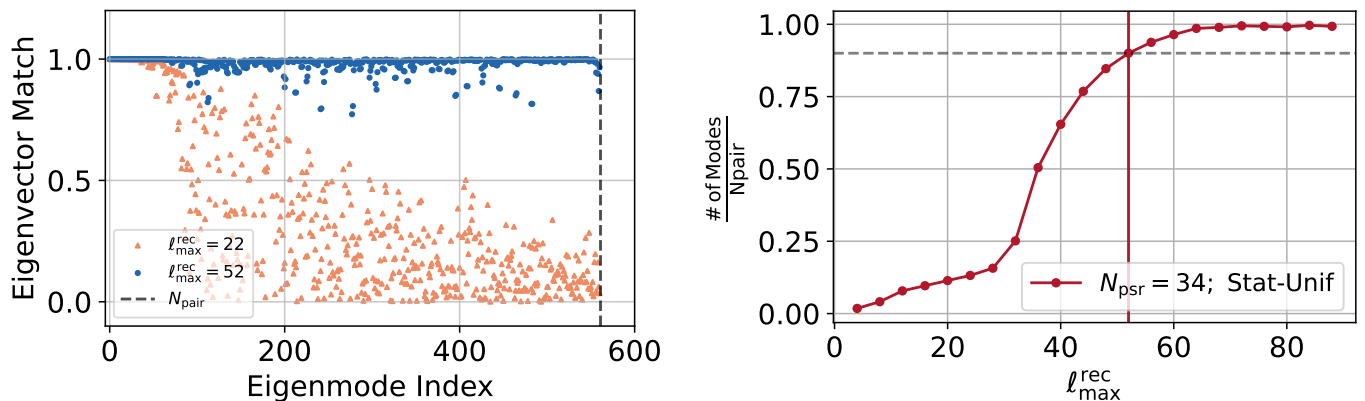


FIG. 4. Left panel: Match between eigenvectors of the Fisher matrix $\mathcal{F}_{ab,cd}$ in the PTR basis, expanded in terms of spherical harmonics for different choices of ℓ_{\max}^{rec} . (The expansion of the eigenvectors of $\mathcal{F}_{ab,cd}$ in terms of pixels having $N_{\text{side}} = 32$ is used as reference.) The spherical harmonic expansion with $\ell_{\max}^{\text{rec}} = 52$ (blue circles) recovers most ($> 90\%$) of the N_{pair} eigenvectors (vertical dashed), while $\ell_{\max}^{\text{rec}} = 22$ (orange triangles) captures only the lowest modes. Right panel: Fraction of eigenmodes with match in the range (0.95,1) normalized by N_{pair} , as a function of ℓ_{\max}^{rec} . The vertical line marks $\ell_{\max}^{\text{rec}} = 52$, the maximum informative angular scale for this configuration corresponding to fraction 0.9 (horizontal dashed grey line). Both of these plots correspond to the PTA configuration shown in Fig. 1.

A. Mode-coupling-induced leakage and ℓ_{\max}^{res}

As discussed in the previous section, $\ell_{\max}^{N_{\text{pair}}}$ does not span the full observable space; therefore setting $\ell_{\max}^{\text{rec}} = \ell_{\max}^{N_{\text{pair}}}$ leads to a loss of important information. To capture most of the informative modes, one should instead adopt $\ell_{\max}^{\text{rec}} \geq \ell_{\max}^{\text{res}}$. To demonstrate these claims, we perform numerical simulations for constructing the angular power spectrum where ℓ_{\max}^{rec} is chosen to equal either $\ell_{\max}^{N_{\text{pair}}}$ or ℓ_{\max}^{res} . The key results from this simulation study are shown in Figs. 5 and 6. The simulations are constructed as follows:

- We consider a PTA configuration consisting of 34 pulsars drawn from a statistically-uniform distribution on the sky, as shown in Fig. 1;
- No pulsar noise is injected, corresponding to an idealized best case scenario;
- We inject a flat angular power spectrum, $C_\ell = 1$ for $0 \leq \ell \leq \ell_{\max}^{\text{gwb}}$, with ℓ_{\max}^{gwb} taking values $\{10, 22, 52, 100, 250\}$.

The blue scatter points in Fig. 5 represent the true angular power spectrum, C_ℓ . For each value of ℓ_{\max}^{gwb} , we generate 100 realizations of the spherical harmonic coefficients $P_{\ell m}$, assuming statistical isotropy (2.4). For each realization, the angular power spectrum is estimated as

$$\tilde{C}_\ell = \frac{1}{2\ell + 1} \sum_m |P_{\ell m}|^2. \quad (4.1)$$

In Fig. 5, the orange dashed line and shaded band show the mean and $\pm 1\sigma$ scatter of \tilde{C}_ℓ over the simulated realizations, respectively, corresponding to the cosmic mean and cosmic variance.

Using these realizations, we simulate the response of the pulsars to the GWB and construct clean map estimators, $\hat{P}_{\ell m}$ following the procedure in Sec. II. The Fisher matrix is regularized by discarding modes with condition number threshold $\kappa = 10^{13}$. The reconstructed angular power spectrum \hat{C}_ℓ is then obtained using (2.13).

For each value of ℓ_{\max}^{gwb} , we compare the reconstructed angular power spectrum for two choices of ℓ_{\max}^{rec} : (i) $\ell_{\max}^{\text{rec}} = \ell_{\max}^{N_{\text{pair}}} = 22$ (red solid), and (ii) $\ell_{\max}^{\text{rec}} = \ell_{\max}^{\text{res}} = 52$ (blue dashed). We observe the following:

- For $\ell_{\max}^{\text{gwb}} = 10$, the reconstruction is unbiased for both $\ell_{\max}^{\text{rec}} = 22$ and $\ell_{\max}^{\text{rec}} = 52$ (left panel of Fig. 5).
- For $\ell_{\max}^{\text{gwb}} = 22$, the reconstruction is slightly negative-biased for $\ell_{\max}^{\text{rec}} = 22$, while a significant negative bias appears for $\ell_{\max}^{\text{rec}} = 52$ (middle panel of Fig. 5).
- For $\ell_{\max}^{\text{gwb}} = 52$, a positive bias appears for $\ell_{\max}^{\text{rec}} = 22$, corresponding to the leakage reported in [4] (right panel of Fig. 5). There is no positive bias for $\ell_{\max}^{\text{rec}} = 52$; the negative bias for $\ell_{\max}^{\text{rec}} = 52$ seen previously for $\ell_{\max}^{\text{gwb}} = 22$ persists.

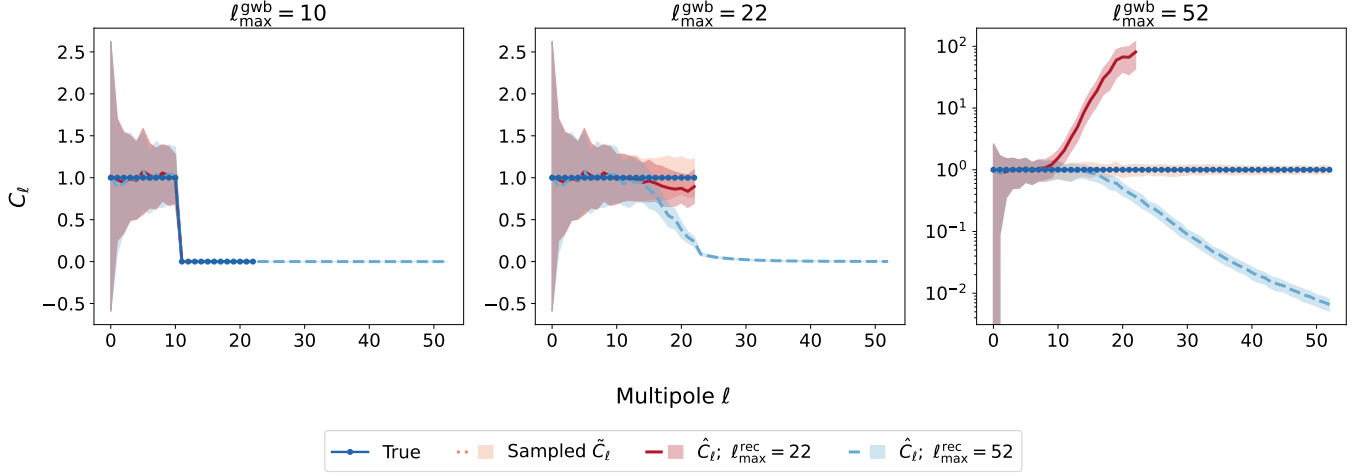


FIG. 5. Demonstration of leakage-induced bias in the reconstructed angular power spectrum \hat{C}_ℓ for the PTA configuration shown in Fig. 1. As ℓ_{\max}^{gwb} increases from 10 to 52 (left to right panels), a significant positive bias appears when truncating recovery at $\ell_{\max}^{\text{rec}} = 22$ (red solid), but not when using $\ell_{\max}^{\text{rec}} = 52$ (blue dashed). The reconstruction is compared with the true (theoretical) C_ℓ (blue dot-solid) and sampled-universe \tilde{C}_ℓ (orange dotted). The shaded region around the estimated \hat{C}_ℓ values denotes $\pm 1\sigma$ cosmic uncertainty.

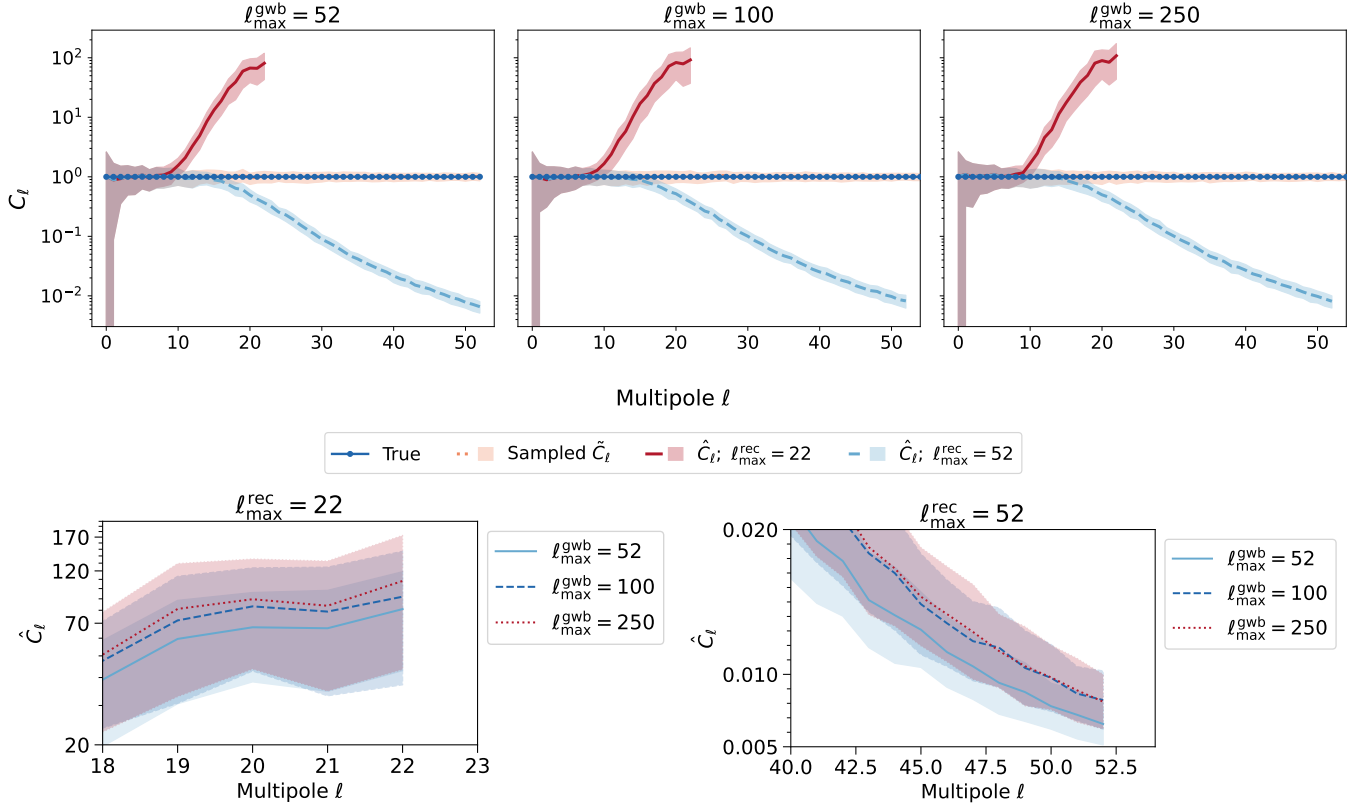


FIG. 6. Top panel: Same as Fig. 5 but for $\ell_{\max}^{\text{gwb}} = 52, 100,$ and 250 , respectively. Increasing ℓ_{\max}^{gwb} beyond 52 does not significantly affect the reconstruction (within cosmic variance), indicating that power at higher multipoles does not propagate through the array. Bottom panel: Comparison of the excess leakage and reduction in the estimated \hat{C}_ℓ values from the top three plots, for $\ell_{\max}^{\text{rec}} = 22$ (bottom left) and $\ell_{\max}^{\text{rec}} = 52$ (bottom right), respectively.

- For larger values of ℓ_{\max}^{gwb} , namely $\ell_{\max}^{\text{gwb}} = 100, 250$ (middle and right panel of the top row of Fig. 6), the positive bias persists for $\ell_{\max}^{\text{rec}} = 22$ with no significant dependence on ℓ_{\max}^{gwb} (the change is within the uncertainty associated

with cosmic variance). This indicates that negligible additional information beyond $\ell_{\max}^{\text{res}} = 52$ makes its way into the angular power spectrum estimates out to $\ell_{\max}^{\text{rec}} = 22$ and $\ell_{\max}^{\text{rec}} = 52$ (see bottom row for zoomed-in and overlaid versions of the top three panels).

These results confirm that the positive bias reported by Semenzato et al. [4] when reconstructing the angular power spectrum originates from unmodeled informative modes when the reconstruction is truncated at $\ell_{\max}^{\text{rec}} = 22$. In [4], the angular scales are divided into “large” and “small” scales using a cutoff defined by $\ell_{\max}^{\text{pair}}$, see (3.5), which is determined solely by the number of pulsars, without taking into accounting their sky distribution.

Our interpretation of their finding is that the excess leakage they are seeing is an artifact of the analysis, arising from the combined effect of multipole coupling and incomplete modeling of the informative angular scales (as hinted at in Ref. [4]). The leakage is primarily due to modes having $\ell_{\max}^{\text{pair}} < \ell \leq \ell_{\max}^{\text{res}}$.

Choosing $\ell_{\max}^{\text{rec}} = 52$ ensures that approximately all the significant information is included, thereby eliminating the leakage-induced bias. In addition, when choosing $\ell_{\max}^{\text{rec}} = 52$ for GWBs having $\ell_{\max}^{\text{gwb}} = 52$ and higher, we are able to recover approximately seven additional C_ℓ values in the range $\ell \in [11, 17]$, consistent with their injected values to within $\pm 1\sigma$ uncertainties, in contrast to the case with $\ell_{\max}^{\text{rec}} = 22$ (top panel of Fig. 6). This provides a further advantage of adopting $\ell_{\max}^{\text{rec}} = 52$.

We note that for $\ell_{\max}^{\text{rec}} = 52$ a negative bias persists in all cases for GW modes beyond $\ell \approx 18$. This bias reflects the partial (and eventually complete) loss of information due to the finite angular resolution of the PTA configuration, as discussed in detail in Sec III A. In the next subsection, we investigate whether it is possible to recover some of this partially lost information by constructing an unbiased estimator for the angular power spectrum.

Importantly, the analytical expressions for the expected value (2.15) of the standard estimator \hat{C}_ℓ , as well as its bias (2.17) and variance (2.18), accurately reproduce the simulation results. This is illustrated in Fig. 7. There we show the expected values of the standard estimator (2.13) of the angular power spectrum $\pm 1\sigma$, with the uncertainty σ calculated from (2.18) for the covariance of the standard estimator. We show results for $\ell_{\max}^{\text{rec}} = 22$ and $\ell_{\max}^{\text{rec}} = 52$, for the specific case $\ell_{\max}^{\text{gwb}} = 52$. For the plots in Fig. 7, we use the same condition number value $\kappa = 10^{13}$ that was used for the simulations shown in Figs. 5 and 6. (A discussion of the impact of different choices of the condition number is given in App. C 1.) Comparison of Fig. 7 with the top-left panel in Fig. 6 demonstrates that our analytical expressions can be used to predict the corresponding quantities for arbitrary pulsar sky distributions, source angular power spectra, and regularization schemes.

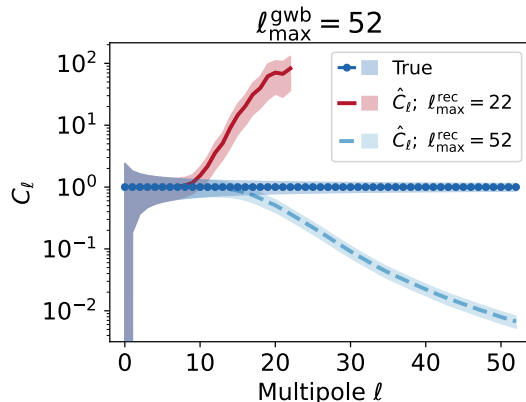


FIG. 7. Similar to the top-left panel of Fig. 6, but using analytical expressions for the expected value of the standard angular power spectrum estimator $\hat{C}_\ell \pm$ and its $\pm 1\sigma$ uncertainty. The agreement of this plot with the top-left panel of Fig. 6 provides a sanity check of our analytic formalism.

Based on the analytical bias matrix \mathbf{M} (2.16), we define an effective maximum multipole ℓ_{eff} , corresponding to the angular scale up to which the angular power spectrum can be reliably recovered. We identify this scale as the multipole at which the diagonal element $M_{\ell\ell}$ drops to half of its maximum value, M_{00} . Since \mathbf{M} depends upon the pulsar geometry and the condition number threshold κ used in calculating the pseudo-inverse of the Fisher matrix \mathcal{F} , the effective multipole ℓ_{eff} is likewise dependent on these choices. For the pulsar array shown in Fig. 1 and $\kappa = 10^{13}$, the analytical bias matrix is shown in the left panel of Fig. 8, with the effective multipole estimated as $\ell_{\text{eff}} \approx 18$ (indicated by vertical line in the top right panel of Fig. 8).

Finally, the analytical bias expression (2.17) shows that, in the absence of mode coupling, no bias is introduced even when $\ell_{\max}^{\text{rec}} < \ell_{\max}^{\text{res}}$ as demonstrated in App. B.

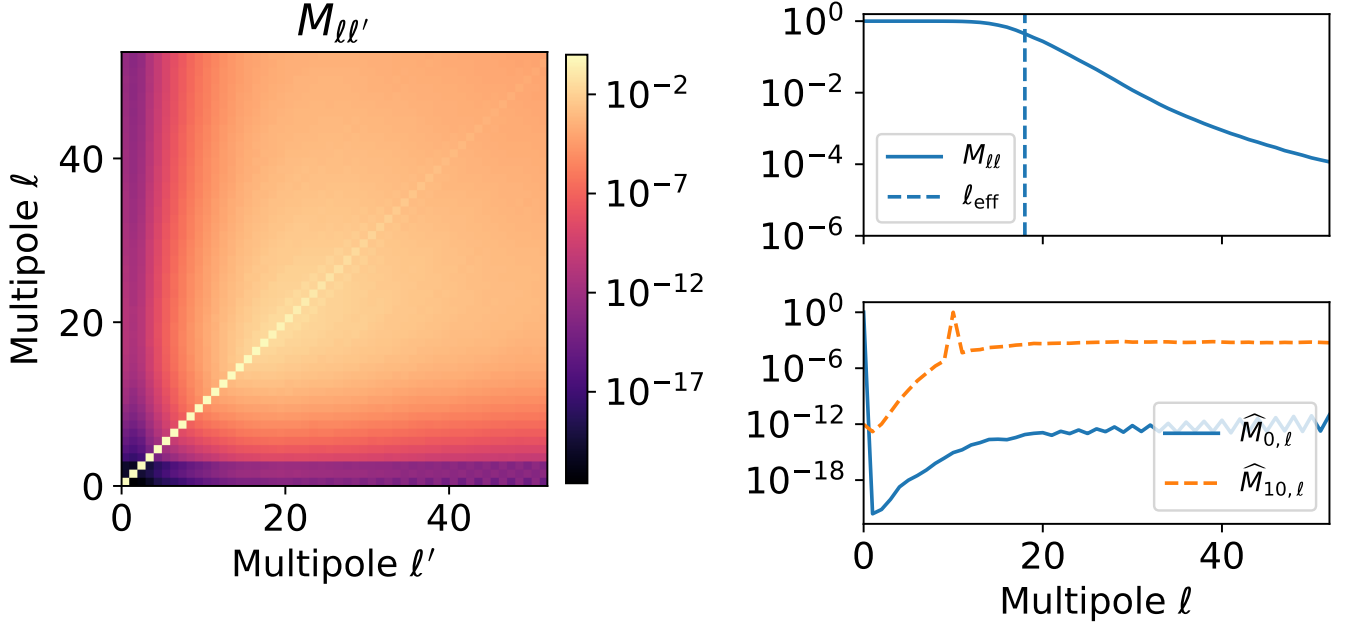


FIG. 8. Left panel: Bias matrix \mathbf{M} (2.16) for the pulsar configuration shown in Fig. 1, with $\ell_{\text{max}}^{\text{rec}} = \ell_{\text{max}}^{\text{gwb}} = 52$ and $\kappa = 10^{13}$. Top right panel: diagonal elements of the matrix, with the vertical line marking the effective multipole ℓ_{eff} (defined as the multipole where $M_{\ell\ell} = M_{00}/2$). Bottom right panel: mode coupling in the normalized bias matrix, $\widehat{M}_{\ell\ell'} \equiv M_{\ell\ell'} / \sqrt{M_{\ell\ell} M_{\ell'\ell'}}$.

B. Debiasing the standard C_ℓ estimator

Imposing the requirement that the angular power spectrum estimator be unbiased, i.e.,

$$\langle\langle \hat{C}_\ell^{(u)} \rangle\rangle_P = C_\ell, \quad (4.2)$$

we define an unbiased estimator

$$\hat{C}_\ell^{(u)} \equiv \sum_{\bar{\ell}'} (M^{-1})_{\ell\bar{\ell}'} \hat{C}_{\bar{\ell}'}, \quad (4.3)$$

where \hat{C}_ℓ and the bias matrix \mathbf{M} are given by (2.13) and (2.16), respectively, see also (2.17). (Note that we have performed debiasing only in the recovered multipole space, summing over ℓ' out to $\ell_{\text{max}}^{\text{rec}}$. Explicitly, we are assuming that there is no prior knowledge of the injected power spectrum for unmodeled scales and that $\ell_{\text{max}}^{\text{gwb}} = \ell_{\text{max}}^{\text{rec}}$.)

But it is important to note that the bias matrix \mathbf{M} may be ill-conditioned (similar to what we saw for the Fisher information matrix \mathcal{F}), necessitating the use of a pseudo-inverse \mathbf{M}^+ for \mathbf{M}^{-1} . This implies that (4.3) should be replaced by

$$\hat{C}_\ell^{(u)} \equiv \sum_{\bar{\ell}'} M_{\ell\bar{\ell}'}^+ \hat{C}_{\bar{\ell}'}, \quad (4.4)$$

which now depends on how we choose to regularize \mathbf{M} . For calculating the pseudo-inverse, we adopt the regularization scheme described in (2.10)-(2.12). Note that this regularization introduces a bias-variance trade off, similar to that discussed earlier in the context of regularizing the Fisher matrix. This means that the resulting estimator depends upon the chosen condition number threshold. The impact of the choice of condition number threshold on C_ℓ recovery for the debiased estimator is discussed in App. C 2.

Using the pseudo-inverse of the bias matrix \mathbf{M} in (4.4) also means that the debiased estimator $\hat{C}_\ell^{(u)}$ is not actually unbiased. It still has a residual bias, which we see when calculating its expected value

$$\langle\langle \hat{C}_\ell^{(u)} \rangle\rangle_P = \sum_{\bar{\ell}'} \sum_{\bar{\ell}''} M_{\ell\bar{\ell}'}^+ M_{\bar{\ell}'\bar{\ell}''} C_{\bar{\ell}''}. \quad (4.5)$$

The rhs of the above expression does not equal $C_{\bar{\ell}}$ since $\mathbf{M}^+\mathbf{M}$ is not the identity matrix. For completeness, it is also relatively straightforward to write down the covariance matrix of the debiased estimators $\hat{C}_{\bar{\ell}}^{(u)}$ and $\hat{C}_{\bar{\ell}'}^{(u)}$:

$$\begin{aligned} \text{Cov}(\hat{C}_{\bar{\ell}}^{(u)}, \hat{C}_{\bar{\ell}'}^{(u)}) &= \sum_{\bar{\ell}_1} \sum_{\bar{\ell}_2} M_{\bar{\ell}\bar{\ell}_1}^+ \text{Cov}(\hat{C}_{\bar{\ell}_1}^{(u)}, \hat{C}_{\bar{\ell}_2}^{(u)}) M_{\bar{\ell}_2, \bar{\ell}'}^+ \\ &= \sum_{\bar{\ell}_1} \sum_{\bar{\ell}_2} \frac{2}{(2\bar{\ell}_1 + 1)(2\bar{\ell}_2 + 1)} \sum_{\bar{m}\bar{m}'} M_{\bar{\ell}\bar{\ell}_1}^+ |\mathcal{C}_{\bar{\ell}_1\bar{m}, \bar{\ell}_2\bar{m}'} + \mathcal{N}_{\bar{\ell}_1\bar{m}, \bar{\ell}_2\bar{m}'}|^2 M_{\bar{\ell}_2, \bar{\ell}'}^+, \end{aligned} \quad (4.6)$$

which follows immediately from (4.4) and the covariance (2.18) of the standard estimator $\hat{C}_{\bar{\ell}}$.

We apply this debiasing procedure to the simulations described in Sec. IV A. We first consider the case $\ell_{\max}^{\text{rec}} = 22$, with results shown in Fig. 9. For this case, the condition number of the bias matrix \mathbf{M} matrix is ~ 1.3 , so no regularization is required. This debiasing procedure is able to correct for the negative bias arising for the case $\ell_{\max}^{\text{gwb}} = 22$ (left panel of Fig. 9), but not for the cases where $\ell_{\max}^{\text{gwb}} > \ell_{\max}^{\text{rec}}$. This indicates that, in the absence of additional spectral information or forward modeling, debiasing alone cannot fully remove the leakage-induced bias.

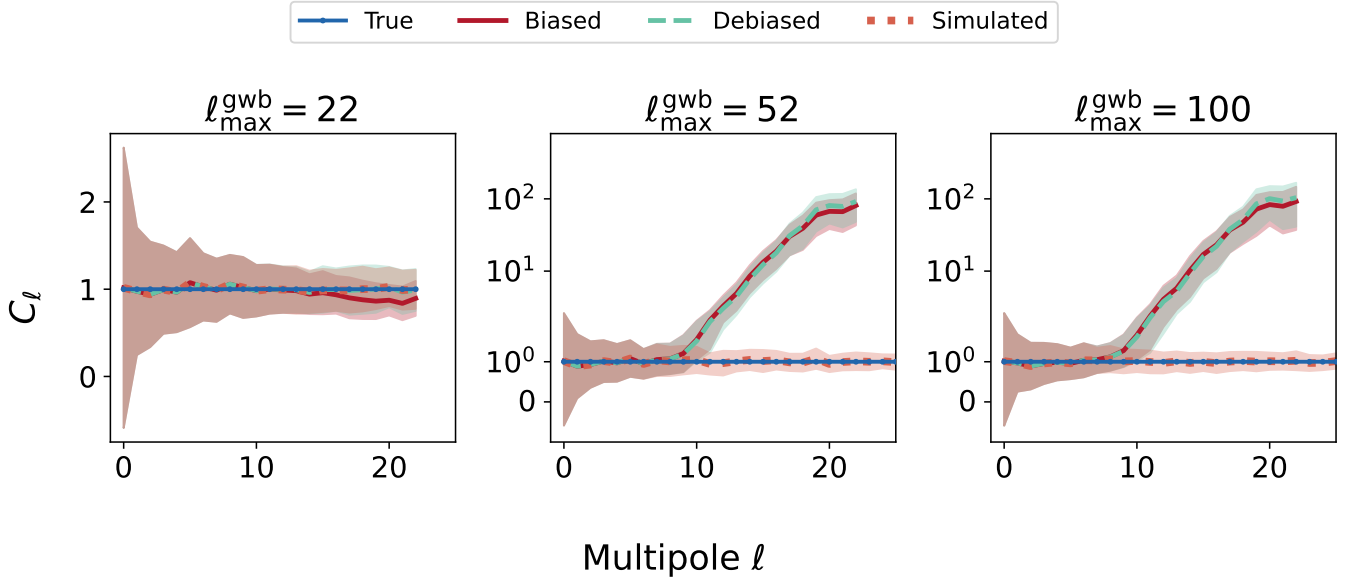


FIG. 9. Debiased angular power spectrum recovery for $\ell_{\max}^{\text{rec}} = 22$. Comparison of the debiased estimator $\hat{C}_{\bar{\ell}}^{(u)}$ (green dashed), the standard estimator $\hat{C}_{\bar{\ell}}$ (red solid), and the injected spectrum (blue dot-solid). The simulation setup is identical to that shown in Figs. 5 and 6. Debiasing corrects the recovery for the $\ell_{\max}^{\text{gwb}} = 22$ case, but does not significantly modify the results for $\ell_{\max}^{\text{gwb}} = 52$ and $\ell_{\max}^{\text{gwb}} = 100$, and the leakage-induced bias persists for multipoles affected by unmolded informative angular scales—i.e., $\ell_{\max}^{\text{rec}} < \ell \leq \ell_{\max}^{\text{res}}$.

We next perform debiasing for the case of $\ell_{\max}^{\text{rec}} = 52$. For this case, \mathbf{M} is not invertible and requires regularization to compute its pseudo-inverse. The recoveries shown in Fig. 10 correspond to a condition number threshold $= 10^4$. Compared to the recovery of the $C_{\bar{\ell}}$'s using the standard estimator, debiasing improves agreement with the injected spectrum for well-resolved multipoles ($\lesssim 22$). The variance increases for $\ell > 22$ corresponding to poorly constrained modes. Results for recoveries of the angular power spectrum for $\ell_{\max}^{\text{rec}} = 52$ for different choices of the condition number threshold are discussed in App. C 2.

We do not show results for $\ell_{\max}^{\text{gwb}} = 10$ and 250 in Figs. 9 and 10 for the following two reasons: (i) for $\ell_{\max}^{\text{gwb}} = 10$, the standard estimator already yields unbiased recovery (left panel of Fig. 5), and debiasing has no effect; and (ii) for $\ell_{\max}^{\text{gwb}} = 250$, the recovered spectrum is consistent within cosmic uncertainty with the cases $\ell_{\max}^{\text{gwb}} = 52$ and 100, as shown in Fig. 6.

Finally, we note that the results of the numerical simulations shown in Figs. 9 and 10 for the debiased estimator $\hat{C}_{\bar{\ell}}^{(u)}$ are consistent with analytic expressions for the expected value and variance of this estimator, given in (4.5) and (4.6). Figure 11 shows $\langle\langle \hat{C}_{\bar{\ell}}^{(u)} \rangle\rangle \pm \sigma_{\bar{\ell}}$, calculated using (4.5) and (4.6) for both $\ell_{\max}^{\text{rec}} = 22$ (left panel) and $\ell_{\max}^{\text{rec}} = 52$ (right panel), for the case $\ell_{\max}^{\text{gwb}} = 52$. The condition number threshold for \mathbf{M} used for the $\ell_{\max}^{\text{rec}} = 52$ plot is 10^4 , which agrees with that used for the plots in Fig. 10. One should compare the left and right panels in Fig. 11 with the

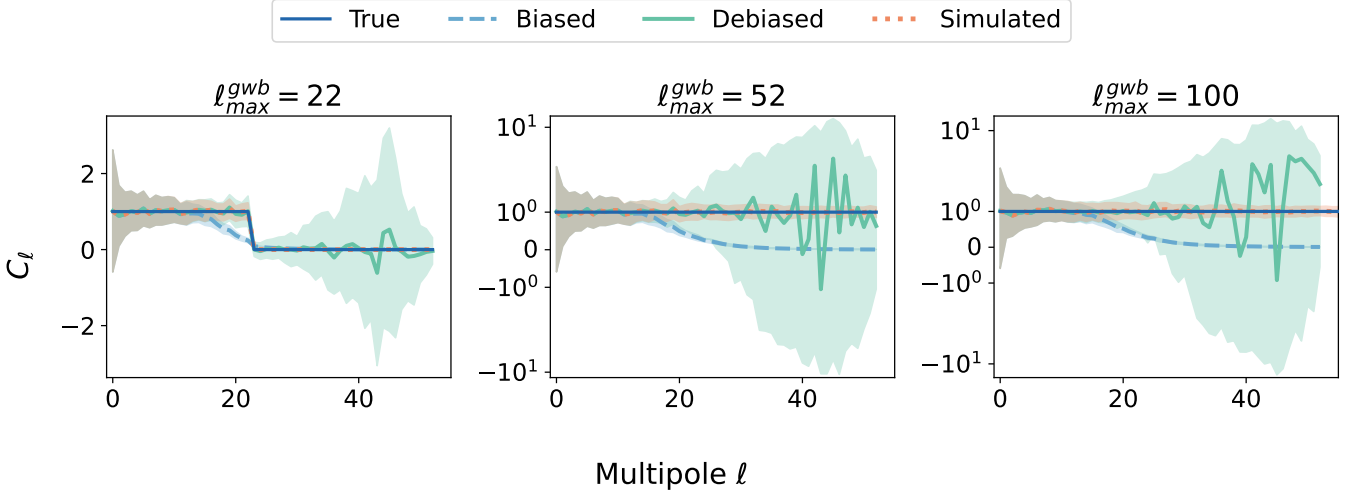


FIG. 10. Similar to Fig. 9 but for $\ell_{\max}^{\text{rec}} = 52$, for simulations shown in Figs. 5 and 6. Mean recovered C_ℓ with $\pm 1\sigma$ uncertainties (shaded bands) compared to the injected spectrum (blue dot-solid). Results are shown for condition number threshold = 10^4 used to construct the pseudo-inverse for the bias matrix \mathbf{M} . Debiasing improves agreement with the injected spectrum for well-resolved multipoles ($\lesssim 22$), while the variance increases for poorly constrained modes (> 22). Figure 16 in App. C 2 illustrates how the choice of condition number threshold impacts the recovery of the angular power spectrum components C_ℓ .

middle panels in Figs. 9 and 10, respectively. As before, the agreement between these plots is a sanity check on the correctness of the analytical expressions for the mean and variance of the debiased estimator.

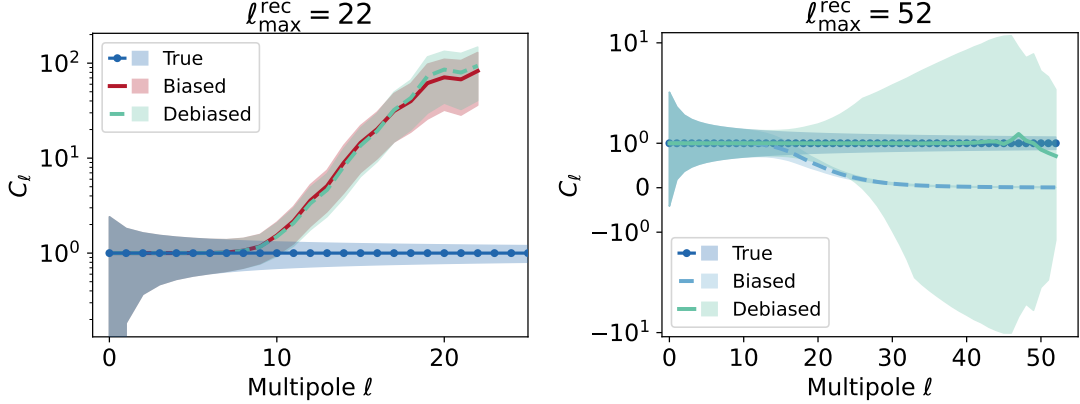


FIG. 11. Similar to the middle panels of Figs. 9 and 10, but using analytical expressions for the expected value of the debiased estimator $\hat{C}_\ell^{(u)}$ of the angular power spectrum \pm its 1σ uncertainty using (4.5) and (4.6). For these plots, $\ell_{\max}^{\text{gwb}} = 52$.

Thus, performing angular power spectrum estimation choosing $\ell_{\max}^{\text{rec}} = \ell_{\max}^{\text{res}}$, together with an optimal choice of the condition number threshold for inverting the Fisher information and bias matrices, leads to an effectively unbiased and leakage-free recovery of the angular power spectrum, in contrast to simply truncating the spherical harmonic analysis at $\ell_{\max}^{\text{Npair}}$.

V. DEPENDENCE ON PTA CONFIGURATION

In the previous section, we showed that the space of “observable skies” for a PTA (i.e., the eigenspace of the corresponding Fisher matrix) is spanned by angular scales up to ℓ_{\max}^{res} , which is generally larger than the theoretical limit $\ell_{\max}^{\text{Npair}}$ set by the number of pulsar pairs. In this Section, we investigate the dependence of ℓ_{\max}^{res} on details of the pulsar configuration—specifically, how ℓ_{\max}^{res} changes when the number of pulsars is held fixed while their sky

distribution varies, or when the number of pulsars is increased while preserving the statistical properties of their spatial distribution.

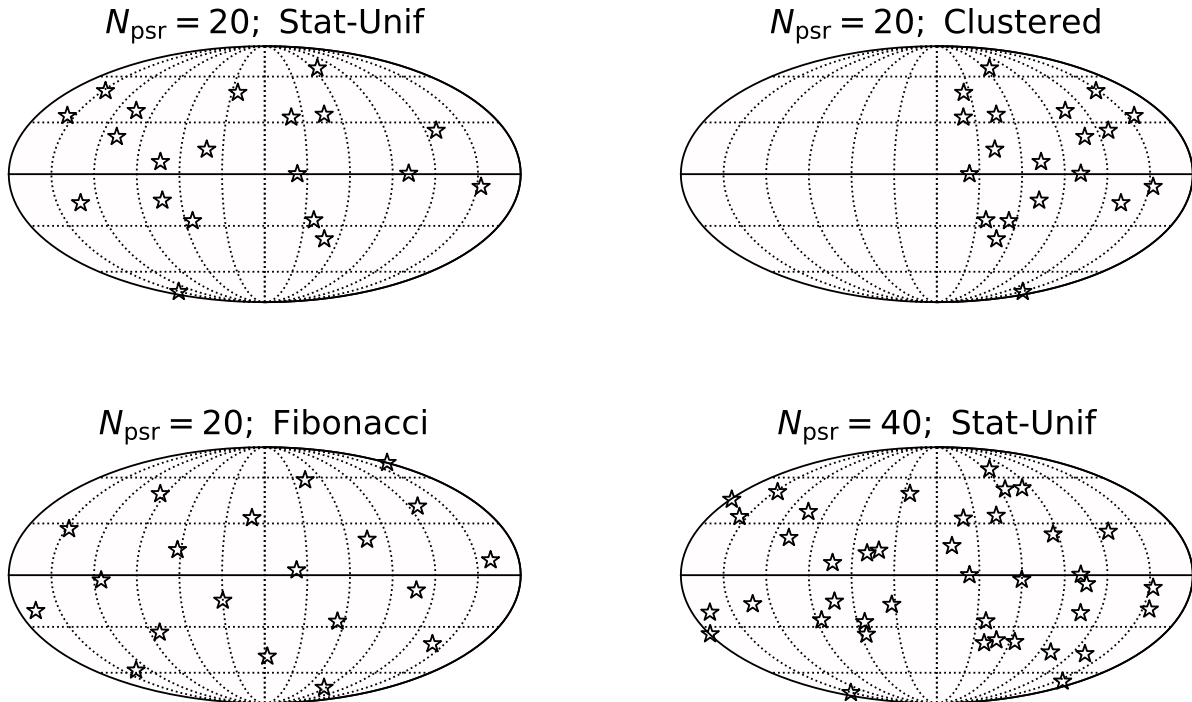


FIG. 12. Sky locations of 20 and 40 pulsars for the four different PTA configurations used for the analyses in Sec. V. The $N_{\text{psr}} = 20$, Clustered configuration is obtained by reflecting the 11 pulsars in the “left hemisphere” of $N_{\text{psr}} = 20$, Stat-Unif configuration to the “right hemisphere”. The $N_{\text{psr}} = 40$, Stat-Unif configuration is obtained by supplementing the $N_{\text{psr}} = 20$, Stat-Unif configuration with 20 additional pulsars drawn from a statistically-uniform distribution on the sky. The $N_{\text{psr}} = 20$, Fibonacci configuration distributes the pulsars on a Fibonacci lattice, yielding a more uniform separation of neighboring pulsars.

To facilitate this investigation, we consider four PTA configurations shown in Fig. 12:

1. $N_{\text{psr}} = 20$, Stat-Unif: 20 pulsars drawn from a statistically-uniform distribution on the sky.
2. $N_{\text{psr}} = 20$, Clustered: 20 pulsars concentrated in a single hemisphere.
3. $N_{\text{psr}} = 20$, Fibonacci: 20 pulsars distributed according to a Fibonacci lattice, yielding a more uniform separation of neighboring pulsars on the sky.
4. $N_{\text{psr}} = 40$, Stat-Unif: 40 pulsars drawn from a statistically-uniform distribution on the sky.

For each configuration, we follow the same procedure as in the previous section to identify $\ell_{\text{max}}^{\text{res}}$. First, we find that the observable space is spanned by spherical harmonic basis functions up to $\ell_{\text{max}}^{\text{res}} > \ell_{\text{max}}^{\text{Npair}}$ in all cases. Second, the value of $\ell_{\text{max}}^{\text{res}}$ depend sensitively on the pulsar sky geometry and the total number of pulsars. These results are shown in Fig. 13 and are summarized in Table II.

Comparing the $N_{\text{psr}} = 20$, Stat-Unif and $N_{\text{psr}} = 20$, Clustered configurations, we find that $\ell_{\text{max}}^{\text{res}}$ is larger for the clustered case. This can be attributed to two effects: (i) the minimum pulsar separation angle for the clustered configuration is smaller than that for the statistically-uniform configuration; and (ii) the concentration of pulsars in one hemisphere leads to enhanced sensitivity over a portion of sky. However, this increased sensitivity comes at the cost of greater non-uniformity in the pulsar array response, which in turn induces stronger multipole coupling (see right panel of Fig. 14) and smaller effective multipole ℓ_{eff} .

Comparing the $N_{\text{psr}} = 20$, Stat-Unif and $N_{\text{psr}} = 20$, Fibonacci configurations, we find that $\ell_{\text{max}}^{\text{Npair}}$ for the Fibonacci configuration provides a much better representation of the observable space and lies closer to $\ell_{\text{max}}^{\text{res}}$ than it does for the statistically-uniform configuration. This is because the Fibonacci lattice yields a nearly uniform sky coverage,

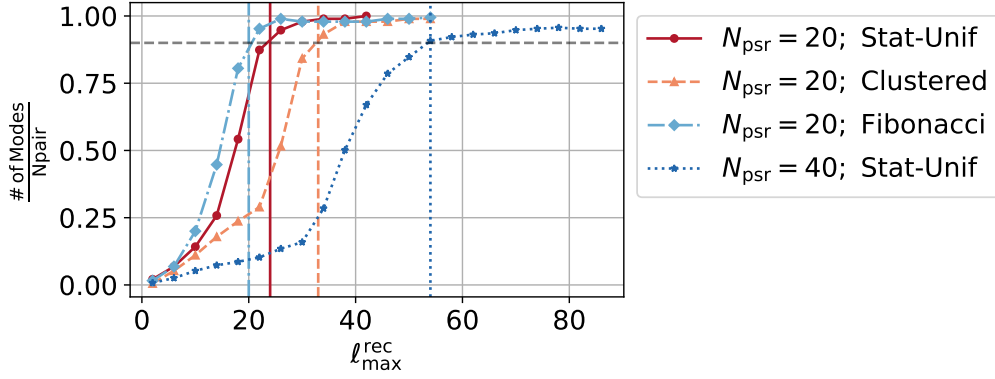


FIG. 13. The fraction of eigenmodes with match in the range $(0.95,1)$ normalized by N_{pair} as a function of $\ell_{\text{max}}^{\text{rec}}$ for the four PTA configurations shown in Fig. 12. The shape of the curve depends on specifics of the pulsar configuration and flattens beyond a characteristic scale. Vertical lines mark $\ell_{\text{max}}^{\text{res}}$, the maximum informative angular scale for each configuration. They have values 20, 24, 33, and 54 corresponding to the 20:Fibonacci, 20:Stat-Unif, 20:Clustered, and 40:Stat-Unif configurations, respectively. See also the 3rd column of Table II.

PTA Configuration	$\ell_{\text{max}}^{N_{\text{pair}}}$	Eigenspace-based		Pulsar-geometry-based		$\frac{\ell_{\text{max}}^{\text{res}}}{\ell_{\text{max}}^{\text{nn}}}$
		$\ell_{\text{max}}^{\text{res}}$	ℓ_{eff}	δ_{nn} (degrees)	$\ell_{\text{max}}^{\text{nn}} = \text{round}\left(\frac{180^\circ}{\delta_{nn}}\right)$	
20 Stat-Unif	12	24	10	15.1	12	2
20 Clustered	12	33	6	12.1	15	2.2
20 Fibonacci	12	20	10	40.4	4	5
40 Stat-Unif	26	54	20	6.89	26	2.07

TABLE II. Summary of PTA configurations and their corresponding angular resolution metrics. For each configuration, we list: (i) the counting-argument-based limit of the maximum reconstructible multipole, $\ell_{\text{max}}^{N_{\text{pair}}}$; (ii) results from the Fisher eigenspace-based analysis—specifically, the maximum informative multipole $\ell_{\text{max}}^{\text{res}}$ and effective multipole ℓ_{eff} ; and (iii) pulsar-geometry-based quantities, including the angular separation δ_{nn} (in degrees) of the nearest-neighbor pulsar pair, and its associated multipole scale $\ell_{\text{max}}^{\text{nn}} \equiv 180/\delta_{nn}$; and (iv) the ratio $\ell_{\text{max}}^{\text{res}}/\ell_{\text{max}}^{\text{nn}}$. Together, these quantities illustrate how pulsar geometry affects the effective angular scales accessible to a PTA.

resulting in weaker multipole coupling (see right panel of Fig. 14). We find that the effective multipole is $\ell_{\text{eff}} = 10$ for both configurations considered.

Next, we compare the $N_{\text{psr}} = 20$, Stat-Unif and $N_{\text{psr}} = 40$, Stat-Unif configurations. As expected, the configuration with a larger number of pulsars results in higher $\ell_{\text{max}}^{\text{res}}$ and ℓ_{eff} . This follows from the increased overall sensitivity (left panel of Fig. 14) and smaller angular separations between pulsars, which allow the array to probe finer angular structures.

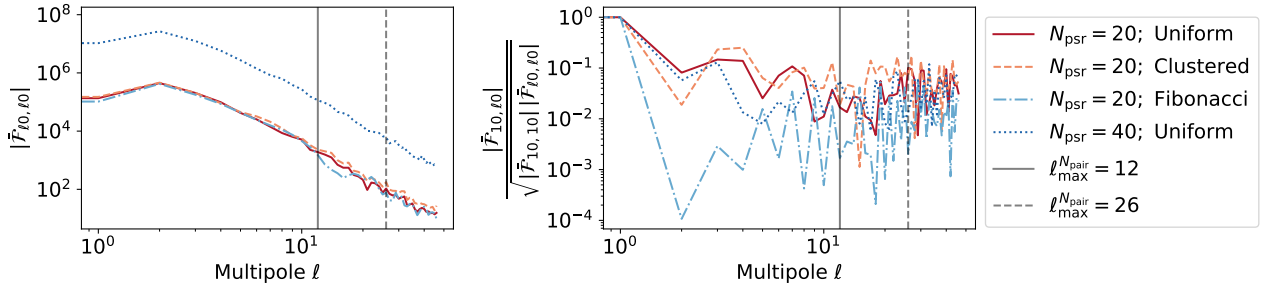


FIG. 14. Plots showing mode suppression (left panel) and mode coupling (right panel) for the different PTA configurations shown in Fig. 12, similar to those shown in Fig. 2.

It is also instructive to examine whether any eigenmodes can be accurately recovered when the reconstruction is performed with $\ell_{\text{max}}^{\text{rec}} < \ell_{\text{max}}^{\text{res}}$. This behavior is illustrated in Fig. 13, which shows the fraction of eigenmodes whose match with the true eigenvectors lies in the range $(0.95,1)$ as a function of $\ell_{\text{max}}^{\text{rec}}$. (See right panel of Fig. 4 for a similar

plot for the $N_{\text{psr}} = 34$, Stat-Unif configuration analyzed in Sec. III.) Comparing the different pulsar configurations having the same number of pulsars (i.e., $N_{\text{psr}} = 20$), we find that the Fibonacci configuration requires the smallest $\ell_{\text{max}}^{\text{rec}}$ to achieve a high fraction, whereas the clustered configuration requires the largest.

Finally, we address whether $\ell_{\text{max}}^{\text{res}}$ can be estimated using simple geometric considerations, such as the angular separation δ_{nn} between the nearest-neighbor pulsar pair, discussed also in [3]. In the noise-free case—where the combined geometric response plays the dominant role—we observe an empirical relation, which is summarized in Table II. Specifically, the ratio between ℓ_{max} values corresponding to the angular separation of the nearest-neighbor pulsar pair and $\ell_{\text{max}}^{\text{res}}$ lies in the range ~ 2 -5. This suggests that basic geometric metrics may provide useful guidance in selecting $\ell_{\text{max}}^{\text{rec}}$ for high-precision pulsar timing experiments, where pulsar geometry is expected to play a more significant role than noise.

VI. SUMMARY / DISCUSSION

In this work, we identified a maximum informative angular scale $\ell_{\text{max}}^{\text{res}}$, by exploiting the information encoded in the Fisher information matrix, and we demonstrated that the commonly used counting-based limit on the maximum reconstructible multipole, $\ell_{\text{max}}^{N_{\text{pair}}} \sim \sqrt{N_{\text{pair}}} - 1$, does not fully capture the true angular resolution of a PTA.

Using both numerical simulations and analytical calculations, we confirmed that truncating spherical harmonic expansions at $\ell_{\text{max}}^{\text{rec}} < \ell_{\text{max}}^{\text{res}}$ leads to leakage from unmodeled yet informative modes, producing the positive bias in the recovered angular power spectrum reported in [4]. We showed that choosing $\ell_{\text{max}}^{\text{rec}} \geq \ell_{\text{max}}^{\text{res}}$ eliminates this leakage-induced bias and increases the number of multipoles recovered with reduced bias. We also demonstrated that GWB power for angular scales beyond $\ell_{\text{max}}^{\text{res}}$ does not significantly affect the reconstruction, consistent with the PTA response acting as a low-pass filter.

We identified a negative bias in the reconstructed angular power spectrum, which reflects the fundamental loss of information due to the finite angular resolution of the array and the resulting blurring of fine-scale sky features. We attempted to mitigate this effect by constructing an unbiased estimator that recovers information from the partially lost modes. While using such an estimator statistically reduced the bias, the variance grows rapidly, signaling the presence of fundamentally unrecoverable multipoles.

We find that due to information loss at small angular scales and mode coupling, the effective number of recoverable modes is smaller than $\ell_{\text{max}}^{\text{res}}$, which we quantify via an effective multipole ℓ_{eff} . The values of $\ell_{\text{max}}^{\text{res}}$ and ℓ_{eff} depend on specifics of the pulsar sky distribution. In Sec. V we further related $\ell_{\text{max}}^{\text{res}}$ empirically to $\ell_{\text{max}}^{\text{nn}}$, constructed from the angular separation of the nearest-neighbor pulsar pair, providing a geometric estimate of a PTA’s maximum informative angular scale.

In the present study, we adopted a “hybrid” approach: the formalism is derived in the noise-dominated limit to motivate the origin of key equations and, most importantly, the form of the Fisher information matrix. We then studied the behavior of $\ell_{\text{max}}^{\text{res}}$ using simulations for a simplified toy model that ignored the presence of noise, in order to establish a best-case (upper-bound) scenario and identify fundamental limiting factors imposed by pulsar geometry alone. This approach also ensures consistency with the noiseless case presented in [4]. Extending this analysis to realistic PTA configurations, including varying pulsar noise, remains an important direction for future work.

Finally, it would also be interesting to further investigate the observed negative bias and alternative methods for constructing unbiased estimators. A more detailed study, involving additional simulations, will be necessary to fully characterize the behavior and performance of such estimators. We plan to explore these questions in forthcoming studies.

ACKNOWLEDGMENTS

We thank Nicola Bellomo, Chiara Mingarelli, Federico Semenzato, Stephen R. Taylor, and Eric Thrane for friendly and fruitful discussions. D.A. and J.D.R. acknowledge financial support from NSF Physics Frontier Center Award PFC-2020265 and start-up funds from the University of Texas Rio Grande Valley.

Some of the results in this paper have been derived using the `healpy` and `HEALPix` packages.

Appendix A: Statistical properties of the frequentist estimators

For completeness, we write down the expectation values and covariances between some key frequentist estimators discussed in the main text:

- Cross-correlations [5]:

$$\begin{aligned}\langle \rho_{ab} \rangle &= \sum_{\ell=0}^{\ell_{\max}^{\text{gwb}}} \sum_{m=-\ell}^{\ell} \gamma_{ab,\ell m} P_{\ell m}, \\ \langle \rho_{ab} \rho_{cd} \rangle - \langle \rho_{ab} \rangle \langle \rho_{cd} \rangle &= \delta_{ac} \delta_{bd} \sigma_{ab}^2.\end{aligned}\tag{A1}$$

- Dirty map:

$$\begin{aligned}\langle X_{\bar{\ell}\bar{m}} \rangle &= \sum_{\ell m} \sum_{a < b} \frac{\gamma_{ab,\bar{\ell}\bar{m}}^* \gamma_{ab,\ell m}}{\sigma_{ab}^2} P_{\ell m} = \sum_{\ell m} \mathcal{F}_{\bar{\ell}\bar{m},\ell m} P_{\ell m}, \\ \langle X_{\bar{\ell}\bar{m}} X_{\bar{\ell}'\bar{m}'}^* \rangle - \langle X_{\bar{\ell}\bar{m}} \rangle \langle X_{\bar{\ell}'\bar{m}'}^* \rangle &= \mathcal{F}_{\bar{\ell}\bar{m},\bar{\ell}'\bar{m}'},\end{aligned}\tag{A2}$$

which follow from (2.5), (2.8), and (A1).

- Clean map:

$$\begin{aligned}\langle \hat{P}_{\bar{\ell}\bar{m}} \rangle &= \sum_{\ell' m'} K_{\bar{\ell}\bar{m},\ell' m'} P_{\ell' m'}, \\ \langle \hat{P}_{\bar{\ell}\bar{m}} \hat{P}_{\bar{\ell}'\bar{m}'}^* \rangle - \langle \hat{P}_{\bar{\ell}\bar{m}} \rangle \langle \hat{P}_{\bar{\ell}'\bar{m}'}^* \rangle &= \mathcal{N}_{\bar{\ell}\bar{m},\bar{\ell}'\bar{m}'},\end{aligned}\tag{A3}$$

where

$$K_{\bar{\ell}\bar{m},\ell' m'} \equiv \sum_{\bar{\ell}'\bar{m}'} \mathcal{F}_{\bar{\ell}\bar{m},\bar{\ell}'\bar{m}'}^+ \mathcal{F}_{\bar{\ell}'\bar{m}',\ell' m'},\tag{A4}$$

$$\mathcal{N}_{\bar{\ell}\bar{m},\bar{\ell}'\bar{m}'} \equiv (\mathcal{F}^+ \cdot \mathcal{F} \cdot \mathcal{F}^{+\dagger})_{\bar{\ell}\bar{m},\bar{\ell}'\bar{m}'},\tag{A5}$$

which follow from (2.9) and (A2). Note that \mathbf{K} is a rectangular matrix if $\ell_{\max}^{\text{rec}} \neq \ell_{\max}^{\text{gwb}}$.

- Noise bias of standard angular power spectrum estimator $\hat{C}_{\bar{\ell}}$:

$$\begin{aligned}\langle\langle \hat{C}_{\bar{\ell}} \rangle\rangle_P &\equiv \frac{1}{2\bar{\ell}+1} \sum_{\bar{m}} \langle\langle \hat{P}_{\bar{\ell}\bar{m}} \hat{P}_{\bar{\ell}\bar{m}}^* \rangle\rangle_P - N_{\bar{\ell}} \\ &= \frac{1}{2\bar{\ell}+1} \sum_{\bar{m}} \left[\langle\langle \hat{P}_{\bar{\ell}\bar{m}} \rangle \langle \hat{P}_{\bar{\ell}\bar{m}}^* \rangle \rangle_P + \mathcal{N}_{\bar{\ell}\bar{m},\bar{\ell}\bar{m}} \right] - N_{\bar{\ell}} \\ &= \frac{1}{2\bar{\ell}+1} \sum_{\bar{m}} \langle\langle \hat{P}_{\bar{\ell}\bar{m}} \rangle \langle \hat{P}_{\bar{\ell}\bar{m}}^* \rangle \rangle_P \\ &= \frac{1}{2\bar{\ell}+1} \sum_{\bar{m}} \sum_{\ell' m'} \sum_{\ell'' m''} K_{\bar{\ell}\bar{m},\ell' m'} K_{\bar{\ell}\bar{m},\ell'' m''}^* \langle P_{\ell' m'} P_{\ell'' m''}^* \rangle_P \\ &= \frac{1}{2\bar{\ell}+1} \sum_{\bar{m}} \sum_{\ell' m'} \sum_{\ell'' m''} K_{\bar{\ell}\bar{m},\ell' m'} K_{\bar{\ell}\bar{m},\ell'' m''}^* C_{\ell'} \delta_{\ell' \ell''} \delta_{m' m''} \\ &= \sum_{\ell'} M_{\bar{\ell}\ell'} C_{\ell'},\end{aligned}\tag{A6}$$

where

$$N_{\bar{\ell}} \equiv \frac{1}{2\bar{\ell}+1} \sum_{\bar{m}} \mathcal{N}_{\bar{\ell}\bar{m},\bar{\ell}\bar{m}}, \quad M_{\bar{\ell}\ell'} \equiv \frac{1}{2\bar{\ell}+1} \sum_{\bar{m} m'} |K_{\bar{\ell}\bar{m},\ell' m'}|^2.\tag{A7}$$

Similar to \mathbf{K} , the bias matrix \mathbf{M} is a rectangular matrix if $\ell_{\max}^{\text{rec}} \neq \ell_{\max}^{\text{gwb}}$.

- Covariance of standard angular power spectrum estimator $\hat{C}_{\bar{\ell}}$:

$$\text{Cov}(\hat{C}_{\bar{\ell}}, \hat{C}_{\bar{\ell}'}) = \frac{2}{(2\bar{\ell}+1)(2\bar{\ell}'+1)} \sum_{\bar{m}\bar{m}'} |c_{\bar{\ell}\bar{m},\bar{\ell}'\bar{m}'} + \mathcal{N}_{\bar{\ell}\bar{m},\bar{\ell}'\bar{m}'}|^2,\tag{A8}$$

where

$$\mathcal{C}_{\bar{\ell}\bar{m},\bar{\ell}'\bar{m}'} \equiv \sum_{\ell m} K_{\bar{\ell}\bar{m},\ell m} K_{\bar{\ell}'\bar{m}',\ell m}^* C_{\ell}, \quad (\text{A9})$$

and $\mathcal{N}_{\bar{\ell}\bar{m},\bar{\ell}'\bar{m}'}$ is given in (A5).

An outline of a proof of (A8) is as follows:

1. It is convenient to first write

$$\hat{P}_{\bar{\ell}\bar{m}} \equiv \mu_{\bar{\ell}\bar{m}} + n_{\bar{\ell}\bar{m}}, \quad \text{where} \quad \mu_{\bar{\ell}\bar{m}} \equiv \langle \hat{P}_{\bar{\ell}\bar{m}} \rangle = \sum_{\ell'm'} K_{\bar{\ell}\bar{m},\ell'm'} P_{\ell'm'} \quad (\text{A10})$$

and $n_{\bar{\ell}\bar{m}}$ is a Gaussian random variable satisfying

$$\langle n_{\bar{\ell}\bar{m}} \rangle = 0, \quad \langle n_{\bar{\ell}\bar{m}} n_{\bar{\ell}'\bar{m}'}^* \rangle = \mathcal{N}_{\bar{\ell}\bar{m},\bar{\ell}'\bar{m}'}. \quad (\text{A11})$$

2. Using (2.4), one can show that

$$\langle \mu_{\bar{\ell}\bar{m}} \rangle_P = 0, \quad \langle \mu_{\bar{\ell}\bar{m}} \mu_{\bar{\ell}'\bar{m}'}^* \rangle_P = \sum_{\ell m} K_{\bar{\ell}\bar{m},\ell m} K_{\bar{\ell}'\bar{m}',\ell m}^* C_{\ell} \equiv \mathcal{C}_{\bar{\ell}\bar{m},\bar{\ell}'\bar{m}'}. \quad (\text{A12})$$

3. Note that $\mu_{\bar{\ell}\bar{m}}$ is a deterministic quantity relative to the $\langle \rangle$ expectation values implying that $\mu_{\bar{\ell}\bar{m}}$ and $n_{\bar{\ell}\bar{m}}$ are statistically independent of one another. (Note also that $n_{\bar{\ell}\bar{m}}$ is a deterministic quantity with respect to the $\langle \rangle_P$ expectation values, but this property is not needed below to calculate the covariance.)
4. Then given the estimator

$$\hat{C}_{\bar{\ell}} = \frac{1}{2\bar{l}+1} \sum_{\bar{m}} |\hat{P}_{\bar{\ell}\bar{m}}|^2 - N_{\bar{\ell}}, \quad (\text{A13})$$

we can calculate the covariance

$$\text{Cov}(\hat{C}_{\bar{\ell}}, \hat{C}_{\bar{\ell}'}) \equiv \langle \langle \hat{C}_{\bar{\ell}} \hat{C}_{\bar{\ell}'} \rangle \rangle_P - \langle \langle \hat{C}_{\bar{\ell}} \rangle \rangle_P \langle \langle \hat{C}_{\bar{\ell}'} \rangle \rangle_P \quad (\text{A14})$$

by first expanding the rhs in terms of expectation values of 4th-order and 2nd-order products of $\hat{P}_{\bar{\ell}\bar{m}}$ and then further expanding those expectation values in terms products of $\mu_{\bar{\ell}\bar{m}}$ and $n_{\bar{\ell}\bar{m}}$.

5. Expectation values $\langle \rangle$ of products of $\mu_{\bar{\ell}\bar{m}}$ and $n_{\bar{\ell}\bar{m}}$ involving an odd number of μ 's or n 's vanish. Expectation values of quadratic or 4th-order products of μ 's or n 's can be evaluated using (A12) and (A11) and Isserlis's theorem [21] (to reduce 4th-order expectation values to products of 2nd-order expectation values). This leads to terms involving products of $\mathcal{N}_{\bar{\ell}\bar{m},\bar{\ell}'\bar{m}'}$ and $\mathcal{C}_{\bar{\ell}\bar{m},\bar{\ell}'\bar{m}'}$.
6. Finally, these terms can be combined using the Hermitian properties of $\mathcal{N}_{\bar{\ell}\bar{m},\bar{\ell}'\bar{m}'}$ and $\mathcal{C}_{\bar{\ell}\bar{m},\bar{\ell}'\bar{m}'}$:

$$\mathcal{N}_{\bar{\ell}\bar{m},\bar{\ell}'\bar{m}'} = \mathcal{N}_{\bar{\ell}'\bar{m}',\bar{\ell}\bar{m}}^* = (-1)^{\bar{m}+\bar{m}'} \mathcal{N}_{\bar{\ell},-\bar{m};\bar{\ell}',-\bar{m}'}^* \quad (\text{A15})$$

and similarly for $\mathcal{C}_{\bar{\ell}\bar{m},\bar{\ell}'\bar{m}'}$, leading to the final result given in (A8).

- Debiased angular power spectrum estimator:

$$\hat{C}_{\bar{\ell}}^{(u)} \equiv \sum_{\bar{\ell}'} M_{\bar{\ell}\bar{\ell}'}^+ \hat{C}_{\bar{\ell}'}, \quad (\text{A16})$$

has expected value and covariance matrix

$$\langle \langle \hat{C}_{\bar{\ell}}^{(u)} \rangle \rangle_P = \sum_{\bar{\ell}'} \sum_{\bar{\ell}''} M_{\bar{\ell}\bar{\ell}'}^+ M_{\bar{\ell}'\bar{\ell}''} C_{\bar{\ell}''}, \quad (\text{A17})$$

$$\text{Cov}(\hat{C}_{\bar{\ell}}^{(u)}, \hat{C}_{\bar{\ell}'}^{(u)}) = \sum_{\bar{\ell}_1} \sum_{\bar{\ell}_2} \frac{2}{(2\bar{\ell}_1+1)(2\bar{\ell}_2+1)} \sum_{\bar{m}\bar{m}'} M_{\bar{\ell}\bar{\ell}_1}^+ |\mathcal{C}_{\bar{\ell}_1\bar{m},\bar{\ell}_2\bar{m}'} + \mathcal{N}_{\bar{\ell}_1\bar{m},\bar{\ell}_2\bar{m}'}|^2 M_{\bar{\ell}_2,\bar{\ell}'}^+, \quad (\text{A18})$$

where the last two equalities follow from (A6) and (A8).

Appendix B: Impact of unmodeled angular scales in the absence of mode coupling

In the main text, we claimed that it is the *combination* of both mode coupling and unmodeled informative angular scales (i.e., choosing $\ell_{\max}^{\text{rec}} < \ell_{\max}^{\text{res}}$) that leads to leakage. To justify that claim, we explicitly show here that if there were no mode coupling, then there would be no leakage even if we choose $\ell_{\max}^{\text{rec}} < \ell_{\max}^{\text{res}}$.

So, let us reconsider the case of a dense-PTA Fisher matrix as in (3.4). For this case, there is no mode coupling, meaning that the Fisher matrix is diagonal in harmonic space:

$$\mathcal{F}_{\ell m, \ell' m'} = \mathcal{F}_\ell \delta_{\ell \ell'} \delta_{m m'} . \quad (\text{B1})$$

Here the indices ℓ and m range over their full range of values for the PTA, i.e., $0 \leq \ell \leq \ell_{\max}^{\text{res}}$. We will assume that $\mathcal{F}_\ell \neq 0$ for all ℓ , so that the pseudo-inverse of the Fisher matrix is just the ordinary inverse:

$$(\mathcal{F}^+)_{\ell m, \ell' m'} = (\mathcal{F}^{-1})_{\ell m, \ell' m'} = \mathcal{F}_\ell^{-1} \delta_{\ell \ell'} \delta_{m m'} , \quad (\text{B2})$$

From (A4), it follows that

$$\begin{aligned} K_{\bar{\ell} \bar{m}, \ell' m'} &\equiv \sum_{\bar{\ell}' \bar{m}'} \mathcal{F}_{\bar{\ell} \bar{m}, \bar{\ell}' \bar{m}'}^+ \mathcal{F}_{\bar{\ell}' \bar{m}', \ell' m'} \\ &= \sum_{\bar{\ell}' \bar{m}'} (\mathcal{F}^{-1})_{\bar{\ell} \bar{m}, \bar{\ell}' \bar{m}'} \mathcal{F}_{\bar{\ell}' \bar{m}', \ell' m'} \\ &= \sum_{\bar{\ell}' \bar{m}'} \mathcal{F}_{\bar{\ell}}^{-1} \delta_{\bar{\ell} \bar{\ell}'} \delta_{\bar{m} \bar{m}'} \mathcal{F}_{\bar{\ell}' \bar{m}', \ell' m'} \\ &= \delta_{\bar{\ell} \ell'} \delta_{\bar{m} m'} \end{aligned} \quad (\text{B3})$$

where the second equality follows from the first equality in (B2); the third equality follows from (B1) and (B2); the fourth equality comes from using the Kronecker deltas $\delta_{\bar{\ell} \bar{\ell}'} \delta_{\bar{m} \bar{m}'}$ to eliminate the sum over $\bar{\ell}' \bar{m}'$. Then the bias matrix \mathbf{M} defined in (A7) becomes

$$M_{\bar{\ell} \ell'} \equiv \frac{1}{2\bar{\ell} + 1} \sum_{\bar{m} m'} |K_{\bar{\ell} \bar{m}, \ell' m'}|^2 = \frac{1}{2\bar{\ell} + 1} \sum_{\bar{m} m'} |\delta_{\bar{\ell} \ell'} \delta_{\bar{m} m'}|^2 = \frac{1}{2\bar{\ell} + 1} \sum_{\bar{m}} \delta_{\bar{\ell} \ell'} = \delta_{\bar{\ell} \ell'} . \quad (\text{B4})$$

Finally, by inspection of (A6) and (2.17), we see that $b_{\bar{\ell}} = 0$. Thus, there is no bias if there is no coupling, even if we choose $\ell_{\max}^{\text{rec}} < \ell_{\max}^{\text{res}}$.

Appendix C: Impact of choice of condition number on C_ℓ reconstruction

As mentioned in the main text, both the standard and debiased estimators ($\hat{C}_{\bar{\ell}}$ and $\hat{C}_{\bar{\ell}}^{(u)}$) of the angular power spectrum involve pseudo-inverses in their definitions. Since calculating a pseudo-inverse depends on the choice of a condition number threshold, so too do the corresponding estimators. In this appendix, we demonstrate the impact of the choice of condition number on the recovery of the $C_{\bar{\ell}}$'s.

1. Standard estimator

We start by discussing the standard estimator $\hat{C}_{\bar{\ell}}$, defined by (2.13), which requires inverting the Fisher information matrix (2.8). Since the Fisher matrix is not invertible, we use its pseudo-inverse \mathcal{F}^+ given by (2.11) and (2.12). The bias and variance of the standard estimator $\hat{C}_{\bar{\ell}}$ can be calculated using (2.17) and (2.18).

The left and right panels of Fig. 15 illustrate the dependence of the bias and variance, respectively, of $\hat{C}_{\bar{\ell}}$ on the choice of condition-number threshold. The plots in this figure correspond to the case where $\ell_{\max}^{\text{rec}} = 52$ and $\ell_{\max}^{\text{gwb}} = 52$. As the condition-number threshold increases from $\kappa = 10^{10}$ to $\kappa = 10^{15}$, the bias decreases while the variance increases. For $\kappa = 10^{17}$, we observe increases in both bias and variance, which we attribute to the amplification of numerical errors. For reference, the analyses presented in Figs. 5, 6, and 7 correspond to the choice $\kappa = 10^{13}$.

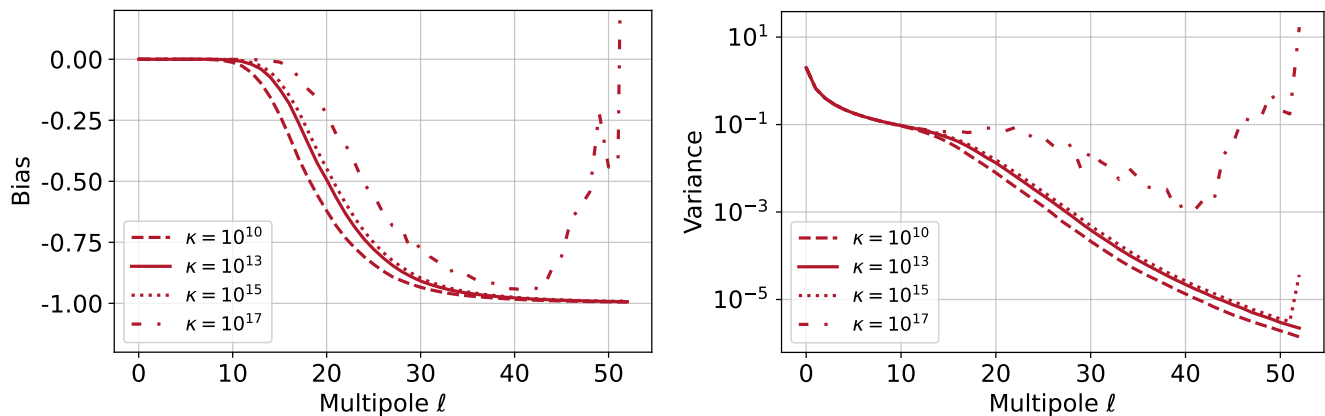


FIG. 15. Dependence of the bias (left panel) and variance (right panel) of the standard estimator \hat{C}_ℓ on the choice of condition number used for calculating the pseudo-inverse of the Fisher matrix. For these plots, we consider the case $\ell_{\max}^{\text{rec}} = 52$ and $\ell_{\max}^{\text{gwb}} = 52$. The negative bias (left panel) reflects information loss due to the finite “width” of the Fisher matrix (or point spread function) in position space. For $\kappa = 10^{17}$, we observe somewhat erratic changes in the bias and variance, which we attribute to the amplification of numerical errors. The analyses presented in Figs. 5, 6, and 7 correspond to the choice $\kappa = 10^{13}$.

2. Debiased estimator

We next discuss the impact of the choice of condition number on C_ℓ reconstruction when using the debiased standard estimator $\hat{C}_\ell^{(u)}$ defined in (A16). For this discussion we will restrict our attention to $\ell_{\max}^{\text{rec}} = 52$, which requires choosing a condition number for two matrix inversions. That is, in addition to choosing a condition number to invert the Fisher matrix \mathcal{F} (as described in the previous subsection), we must also choose a condition number to invert the bias matrix \mathbf{M} , which is shown in the left panel of Fig. 8. Here, we will fix $\kappa = 10^{13}$ for inverting the Fisher matrix (as described above), and examine four different choices of the condition-number threshold for inverting \mathbf{M} , which are $\{10, 10^2, 10^3, 10^4\}$.

The results are presented in Fig. 16, where rows from top to bottom correspond to increasing condition-number threshold for \mathbf{M} . We also consider three different values of $\ell_{\max}^{\text{gwb}} \in \{22, 52, 100\}$, corresponding to the three different columns in the plot. For a condition-number threshold of 10 (top row), the debiased estimator shows clear improvement relative to the standard estimator, with approximately five additional multipoles consistent with the injected spectrum within $\pm 1\sigma$ uncertainty (second panel). However, as the condition number threshold is increased (lower rows), we find that although the debiased estimator formally starts to become statistically unbiased, the variance grows rapidly, leading to increasingly noisy reconstructions. This behavior indicates that modes beyond $\ell \approx 22$ are intrinsically difficult to recover.

-
- [1] Yacine Ali-Haïmoud, Tristan L. Smith, and Chiara M. F. Mingarelli. Fisher formalism for anisotropic gravitational-wave background searches with pulsar timing arrays. *Phys. Rev. D*, 102:122005, Dec 2020. doi:10.1103/PhysRevD.102.122005. URL <https://link.aps.org/doi/10.1103/PhysRevD.102.122005>.
 - [2] Yacine Ali-Haïmoud, Tristan L. Smith, and Chiara M. F. Mingarelli. Insights into searches for anisotropies in the nanohertz gravitational-wave background. *Phys. Rev. D*, 103:042009, Feb 2021. doi:10.1103/PhysRevD.103.042009. URL <https://link.aps.org/doi/10.1103/PhysRevD.103.042009>.
 - [3] Kathrin Grunthal, David J. Champion, Eric Thrane, Rowina S. Nathan, Michael Kramer, and Matthew T. Miles. Optimising gravitational-wave sky maps for pulsar timing arrays. *Astronomy & Astrophysics*, 2026. doi:10.1051/0004-6361/202557896. In press.
 - [4] Federico Semenzato, Nicola Bellomo, Alvisè Raccanelli, and Chiara M. F. Mingarelli. Bias from small-scale leakage in Pulsar Timing Array maps. 10 2025.
 - [5] Nihan Pol, Stephen R. Taylor, and Joseph D. Romano. Forecasting Pulsar Timing Array Sensitivity to Anisotropy in the Stochastic Gravitational Wave Background. *Astrophys. J.*, 940(2):173, 2022. doi:10.3847/1538-4357/ac9836.
 - [6] Gabriella Agazie et al. The NANOGrav 15 yr Data Set: Search for Anisotropy in the Gravitational-wave Background. *Astrophys. J. Lett.*, 956(1):L3, 2023. doi:10.3847/2041-8213/acf4fd.
 - [7] R. W. Hellings and G. S. Downs. Upper limits on the isotropic gravitational radiation background from pulsar timing analysis. *Astrophys. J.*, 265:L39–L42, February 1983. doi:10.1086/183954.

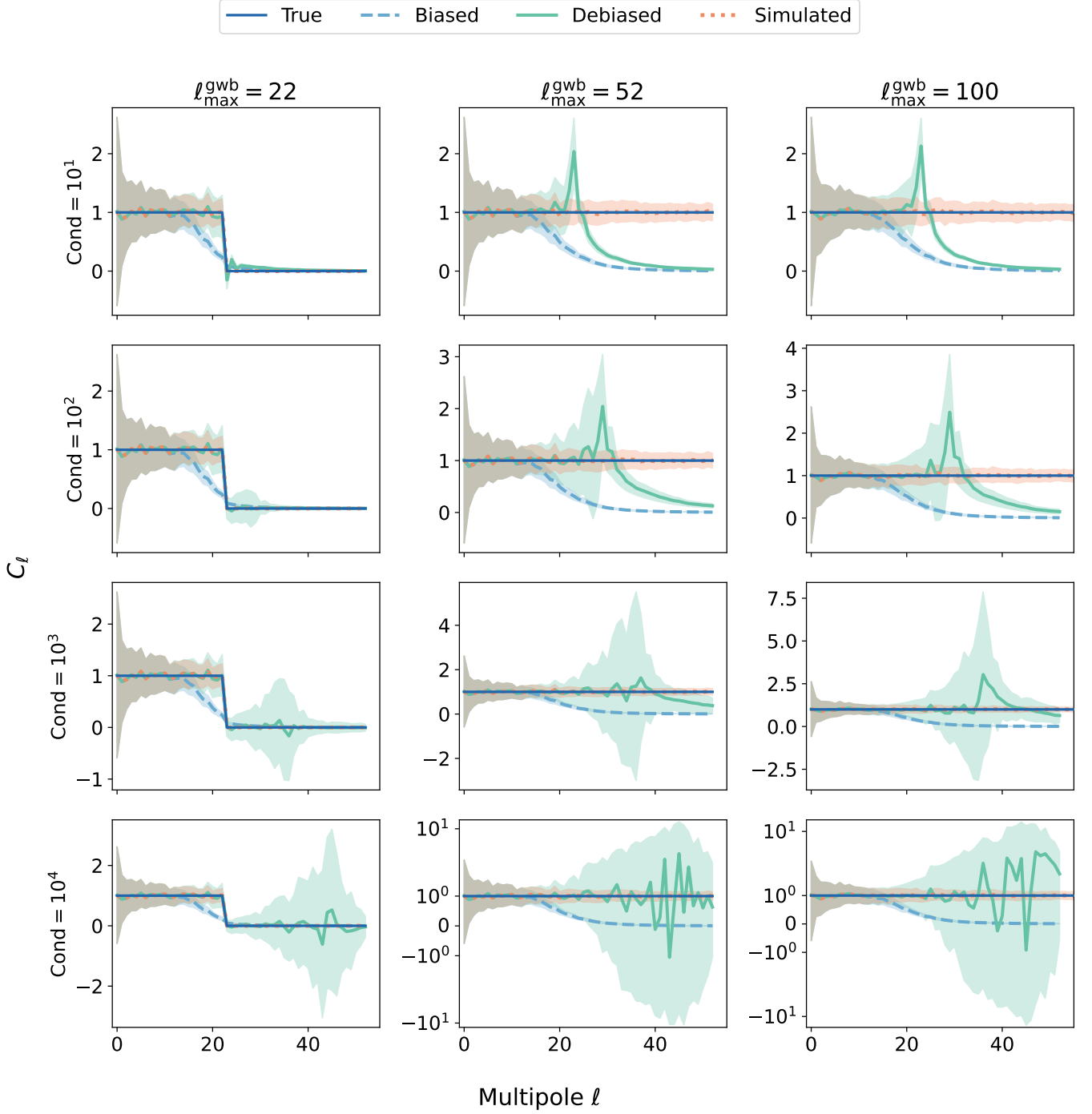


FIG. 16. Similar to Fig. 10 (for $\ell_{\max}^{\text{rec}} = 52$) for different values of the condition-number threshold $\{10, 10^2, 10^3, 10^4\}$ (different rows, top to bottom) used to construct the pseudo-inverse for the bias matrix M . The mean recovered C_ℓ with $\pm 1\sigma$ uncertainties (shaded bands) are compared to the injected spectrum (blue dot-solid). Debiasing improves agreement with the injected spectrum for well-resolved multipoles ($\lesssim 22$). As the threshold increases, the bias reduces but the variance increases for poorly constrained modes (> 22).

- [8] N. Christensen. *On Measuring the Stochastic Gravitational Radiation Background with Laser Interferometric Antennas*. PhD thesis, Massachusetts Institute of Technology, 1990.
- [9] Nelson Christensen. Measuring the stochastic gravitational-radiation background with laser-interferometric antennas. *Phys. Rev. D*, 46:5250–5266, Dec 1992. doi:10.1103/PhysRevD.46.5250. URL <https://link.aps.org/doi/10.1103/PhysRevD.46.5250>.

- [10] Éanna É. Flanagan. Sensitivity of the Laser Interferometer Gravitational Wave Observatory to a stochastic background, and its dependence on the detector orientations. *Phys. Rev. D*, 48:2389, 1993.
- [11] C. M. F. Mingarelli, T. Sidery, I. Mandel, and A. Vecchio. Characterizing gravitational wave stochastic background anisotropy with pulsar timing arrays. *Phys. Rev. D*, 88(6):062005, September 2013. doi:10.1103/PhysRevD.88.062005.
- [12] Sanjit Mitra, Sanjeev Dhurandhar, Tarun Souradeep, Albert Lazzarini, Vuk Mandic, Sukanta Bose, and Stefan Ballmer. Gravitational wave radiometry: Mapping a stochastic gravitational wave background. *Phys. Rev. D*, 77:042002, 2008. doi:10.1103/PhysRevD.77.042002.
- [13] Eric Thrane, Stefan Ballmer, Joseph D. Romano, Sanjit Mitra, Dipongkar Talukder, Sukanta Bose, and Vuk Mandic. Probing the anisotropies of a stochastic gravitational-wave background using a network of ground-based laser interferometers. *Phys. Rev. D*, 80:122002, 2009. doi:10.1103/PhysRevD.80.122002.
- [14] Kathrin Grunthal et al. The MeerKAT Pulsar Timing Array: Maps of the gravitational wave sky with the 4.5-yr data release. *Mon. Not. Roy. Astron. Soc.*, 536(2):1501–1517, 2024. doi:10.1093/mnras/stae2573.
- [15] Deepali Agarwal, Jishnu Suresh, Sanjit Mitra, and Anirban Ain. Angular power spectra of anisotropic stochastic gravitational wave background: Developing statistical methods and analyzing data from ground-based detectors. *Phys. Rev. D*, 108:023011, Jul 2023. doi:10.1103/PhysRevD.108.023011. URL <https://link.aps.org/doi/10.1103/PhysRevD.108.023011>.
- [16] Joseph D. Romano and Neil J. Cornish. Detection methods for stochastic gravitational-wave backgrounds: a unified treatment. *Living Rev. Rel.*, 20(1):2, 2017. doi:10.1007/s41114-017-0004-1.
- [17] Valerie Domcke, Gabriele Franciolini, and Mauro Pieroni. Cosmic Variance in Anisotropy Searches at Pulsar Timing Arrays. 8 2025.
- [18] Note1. <http://healpix.sf.net>.
- [19] K. M. Górski, E. Hivon, A. J. Banday, B. D. Wandelt, F. K. Hansen, M. Reinecke, and M. Bartelmann. HEALPix: A Framework for High-Resolution Discretization and Fast Analysis of Data Distributed on the Sphere. *Astrophys. J.*, 622:759–771, April 2005. doi:10.1086/427976.
- [20] Andrea Zonca, Leo Singer, Daniel Lenz, Martin Reinecke, Cyrille Rosset, Eric Hivon, and Krzysztof Gorski. healpy: equal area pixelization and spherical harmonics transforms for data on the sphere in python. *Journal of Open Source Software*, 4(35):1298, March 2019. doi:10.21105/joss.01298. URL <https://doi.org/10.21105/joss.01298>.
- [21] L. Isserlis. On a formula for the product-moment coefficient of any order of a normal frequency distribution in any number of variables. *Biometrika*, 12(1-2):134–139, 11 1918. ISSN 0006-3444. doi:10.1093/biomet/12.1-2.134. URL <https://doi.org/10.1093/biomet/12.1-2.134>.